

IGM metal enrichment through dust sputtering

Simone Bianchi¹ and Andrea Ferrara²

¹ *Istituto di Radioastronomia / CNR - Sezione di Firenze, Largo Enrico Fermi 5, 50125 Firenze, Italy*

² *SISSA/International School for Advanced Studies, via Beirut 2-4, 34013 Trieste, Italy*

January 2005

ABSTRACT

We study the motion of dust grains into the Intergalactic Medium (IGM) around redshift $z = 3$, to test the hypothesis that grains can efficiently pollute the gas with metals through sputtering. We use the results available in the literature for radiation-driven dust ejection from galaxies as initial conditions, and follow the motion onward. Via this mechanism, grains are ejected into the IGM with velocities $> 100 \text{ km s}^{-1}$; as they move supersonically, grains can be efficiently eroded by *non-thermal* sputtering. However, Coulomb and collisional drag forces effectively reduce the charged grain velocity. Up-to-date sputtering yields for graphite and silicate (olivine) grains have been derived using the code TRIM, for which we provide analytic fits. After training our method on a homogeneous density case, we analyze the grain motion and sputtering in the IGM density field as derived from a Λ CDM cosmological simulation at $z = 3.27$. We found that only large ($a \gtrsim 0.1\text{-}\mu\text{m}$) grains can travel up to considerable distances (few $\times 100$ kpc physical) before being stopped. Resulting metallicities show a well defined trend with overdensity δ . The maximum metallicities are reached for $10 < \delta < 100$ (corresponding to systems, in QSO absorption spectra, with $14.5 < \log N(\text{H I}) < 16$). However the distribution of sputtered metals is very inhomogeneous, with only a small fraction of the IGM volume polluted by dust sputtering (filling factors of 18 per cent for Si and 6 per cent for C). For the adopted size distribution, grains are never completely destroyed; nevertheless, the extinction and gas photo-electric heating effects due to this population of intergalactic grains are well below current detection limits.

Key words: dust, extinction - intergalactic medium - cosmology: miscellaneous

1 INTRODUCTION

In recent years, the possible presence of dust in the IGM has received new attention. Before the observations of CMB anisotropies (de Bernardis & et al. 2000; Spergel et al. 2003) strengthened the hypothesis of a flat, Λ -dominated universe, an explanation alternative to cosmology was proposed for the dimming of distant ($z \approx 0.5$) Type Ia SNe (Riess et al. 1998; Perlmutter et al. 1999): obscuration from intergalactic dust may have been responsible for the observations, provided that dust grains had a *grey* extinction law (as for elongated or large grains; Aguirre 1999b,a) and a smooth distribution tracing the lower density intergalactic gas (Croft et al. 2000). Although now the cosmologic origin for the dimming is preferred, dust is still considered to be an important component of the extragalactic medium. Besides the most commonly studied extinction effects, dust may affect, for instance, the thermal balance of the gas, being an effective heating agent in low density environments (through photoelectric heating; Nath et al. 1999; Inoue & Kamaya 2003, 2004) and providing a source

for cooling in the denser, higher temperature Intracluster Medium (via IR emission; Montier & Giard 2004).

Furthermore, dust is studied for its own nature. About half of the metals in the Milky Way and in other local galaxies is locked up in dust grains (Whittet 1992; James et al. 2002). Though originating in stars, metals are also present in the low density IGM, far from production sites. Metal lines are now routinely found associated to hydrogen in the $z = 3$ Ly α forest for column densities as low as $N(\text{H I}) < 10^{14.5}$, corresponding to gas only 10 times more dense than the cosmic mean (Cowie & Songaila 1998; Ellison et al. 2000; Schaye 2001). The most popular mechanism to explain the metal pollution of the IGM is galactic winds from supernovae explosions: metal enriched gas is blown out from (proto-)galaxies into an IGM with pristine conditions (Madau et al. 2001; Aguirre et al. 2001c,b). As an alternative, Ferrara et al. (1991) and Aguirre et al. (2001a,c) have proposed that metals could be expelled from galaxies as radiation-pressure driven grains. Grains then release metals in the IGM through sputtering. Not only this mechanism can in principle provide for the same levels of metallicity as the galactic winds hypothesis, but the attractive feature of

this model is that, unlike winds, enrichment by dust would not impact the thermal/structural properties of the IGM, as no shock waves are involved in the transport. In addition, metals transported via this process are associated with cool gas, alleviating the need to explain how this can be achieved if metals are transported by the hot gas produced by SN shocks.

In spite of such interesting features several questions await a quantitative answer: how far can dust grains travel in the IGM? What is the dominant sputtering mechanism? How much dust is needed to produce the observed metallicity? These are the basic answers we are aiming at obtaining in the present work.

A few authors have studied the ejection of dust grains from galaxies due to the radiation pressure from the galaxy's starlight. References to these works are given in § 2. Although no estimate is made about what fraction of the total dust content is ejected, most works agree that escaping grains will be able to overcome the gravitational attraction reaching large velocities, $v \gtrsim 100 \text{ km s}^{-1}$. When colliding with gas particles, the kinetic energy of the impact is comparable to the thermal energy of a gas with temperature $T \approx 10^6 \text{ K}$. Thus, *non-thermal* sputtering may be a viable mechanism to erode grains and deposit their constituents (metals), even in the low temperature (and density) gas. In this paper, we will assume that a fraction of galactic dust grains will be able to go beyond the virial radius of a galaxy, with velocities and radii as inferred from literature. From this point onward the grain is slowed down by drag forces: we include both collisional drag and Coulomb drag (due to the ionised nature of the medium and the charge a grain attains when exposed to the metagalactic UV background). During the grain motion, metals are deposited in the IGM as a result of sputtering (we consider both thermal and non-thermal processes). Our approach is different from that of Aguirre et al. (2001a,c), as they assume that dust grains can reach the equilibrium point between gravitation and radiation pressure and they include thermal sputtering only.

The paper is organised as follows: in § 2 we summarise the literature results on dust ejection from galaxies, which we use as initial conditions in our computation; § 3 describe the physics we have adopted to describe the grain motion, charging and sputtering. Results are presented and discussed in § 4 for the ideal case of a homogeneous density field; the method is then applied to a more realistic simulated cosmological density field in § 5. In § 6 we will compare our results with previous works. Finally, we summarise our results in § 7¹.

2 DUST EJECTION FROM GALAXIES

Following the motion of dust grains from their formation sites in a galactic disk to the outer reaches of the halo is a

complex task. It involves the evaluation of: radiation pressure and other forces resulting from anisotropic radiation fields (Weingartner & Draine 2001b), possibly taking into account the opacity of the dusty disk (Davies et al. 1998); disk and halo gravity; gas drag (and the grain charge; see next Section); sputtering rates; magnetic forces; geometry and physical condition in a multiphase disk and halo gas.

A few authors have studied the dust expulsion, including most (but not all) of the relevant processes. We summarise here their findings.

(i) Depending on their size and composition, some dust grains can escape the halo of the galaxy in a relatively short time (a few hundreds Myr). These escaping grains attain terminal velocities of about $100\text{-}1000 \text{ km s}^{-1}$ (Ferrara et al. 1991; Ferrara 1997; Shustov & Vibe 1995; Simonsen & Hannestad 1999).

(ii) Escaping grains are relatively large, with sizes in the range $0.05\text{-}0.2 \mu\text{m}$. Larger grains are too heavy to escape the gravitational well, while smaller grains offer smaller efficiencies to radiation pressure and do not travel far from their formation site (Shustov & Vibe 1995; Davies et al. 1998). Furthermore, smaller and slower grains could be more effectively eroded by sputtering, as they spend more time in the hot halo environment (Ferrara et al. 1991; Shustov & Vibe 1995). Instead, velocities for escaping grains do not depend much on the grain size (Simonsen & Hannestad 1999).

(iii) Being heavier and having smaller radiation pressure efficiencies, silicate grains reach smaller velocities than graphite grains and may be underrepresented among the escaping grains (Barsella et al. 1989; Ferrara et al. 1990, 1991).

Unfortunately, none of these works provide a statistic for the properties and amount of escaping grains. Apart from a few illustrative cases, here we will simply assume that sizes are in the range $0.05 < a [\mu\text{m}] < 0.2$ and velocities in the range $100 < v [\text{km s}^{-1}] < 1000$, with all values of a and v equally represented. Typically, dust grains in a galaxy are believed to obey a power law size distribution, $n(a) \propto a^{-3.5}$, and to have a ratio 1:1 for the relative proportion of graphite and silicate grains (i.e. the MRN model for Milky Way dust; Mathis, Rumpl & Nordsiek 1977; Draine & Lee 1984). For a given dust mass, the MRN model sets the number of grains for each radius bin, with smaller grains being obviously more represented. By adopting a flat distribution for the sizes of the grains that eventually escape in the IGM (i.e. with the same number of large and small grains), we implicitly assume that a good fraction of the dust mass is trapped inside the galaxy. Even allowing all large grains to be ejected, at maximum only about 10 per cent of the dust mass can travel to the IGM. Thus, we use 10 per cent as an upper limit to the fraction of a galaxy's dust mass that can be ejected. The limit has been derived for the MRN graphite and silicate abundance ratio 1:1, that we adopt also for ejected grains. As literature results suggest a lower efficiency for ejection of silicate grains, this ratio may constitute an upper limit to the presence of silicate grains in the IGM, if the assumption of MRN-like dust inside a galaxy is valid.

Unfortunately, size and material distributions for dust in external galaxies are quite uncertain, especially at high redshift. In the early universe, dust can be efficiently produced only by Type II supernovae (Todini & Ferrara 2001).

¹ Throughout this paper we will assume a flat universe with total matter, vacuum, and baryonic densities in units of the critical density of $\Omega_m = 0.3$, $\Omega_\Lambda = 0.7$, and $\Omega_b h^2 = 0.028$, respectively, and a Hubble constant of $H_0 = 100 h \text{ km s}^{-1} \text{ Mpc}^{-1}$, with $h = 0.7$. The parameters defining the linear dark matter power spectrum are $\sigma_8 = 0.9$, $n = 0.93$, $dn/d \ln k = 0$ (Spergel et al. 2003)

For pristine conditions of the parental cloud, dust is produced in pair-instability supernovae from massive (140-260 M_{\odot}) stellar progenitors: models predict in this case a preferential formation of silicate grains (Nozawa et al. 2003; Schneider et al. 2004) although considerable masses of carbon can be locked up in dust if the CO molecule formation is duly taken into account (Schneider et al. 2004). As the gas metallicity rises above a critical value ($\gtrsim 10^{-5} Z_{\odot}$; Schneider et al. 2003) the formation of very massive star is suppressed and dust forms in the ejecta of core-collapse supernovae: in this case, similar masses of carbon and silicate grains can form (Todini & Ferrara 2001). For both kind of objects, the cumulative size distribution over all the materials formed in the ejecta can be roughly described by a power law; in particular, large grains tend to follow the MRN distribution (Nozawa et al. 2003). Thus, we believe the upper limits derived above for the amount of dust ejected into the IGM are reasonable estimates.

3 PHYSICS OF DUST GRAINS IN THE IGM

In this Section we present the basic physical ingredients we have adopted to describe the motion, charging and sputtering processes for dust in the IGM. We will consider a gas with pristine composition (76 per cent H, 24 per cent He in mass). Before considering a cosmological density field, we will show some illustrative cases for the mean density at $z = 3$. For the adopted cosmology, the mean baryonic density at $z = 3$ is $\rho_b = 2.3 \times 10^{-29} \text{ g cm}^{-3}$ (equivalent to $n_H = 1.0 \times 10^{-5} \text{ cm}^{-3}$). As for the gas temperature, we have adopted $T = 2 \times 10^4 \text{ K}$, a typical value derived for the low density IGM from QSOs absorption lines (Schaye et al. 2000). As we allow for different ionization fractions, six different kind of particles may be present in the IGM: neutral and ionised hydrogen (H I, H II), neutral, single and double ionised helium (He I, He II, He III) and electrons.

We will find useful to express the grain velocity v through the atomic speed ratio

$$s_i = \left(\frac{m_i v^2}{2KT} \right)^{1/2},$$

where m_i is the mass of each particle constituting the gas. It is $s_H = s_{He}/2 = \sqrt{m_H/m_e} \approx 42.8 s_e$. We saw in § 2 that escaping grains achieve a certain terminal velocity as a balance between radiation pressure and the other forces opposing the motion. That velocity will be considered as the initial velocity of the grain in the IGM, and we will follow the motion assuming that dust is slowed down because of gas drag (§ 3.1). For simplicity, the gas drag is the only force included in our study. This is clearly an approximation when studying the motion of a grain in a inhomogeneous density field (§ 5). In that case we should also consider the path deviations due to gravitational attraction by denser regions; if the encountered overdensities are forming stars, radiation pressure and other forces resulting from anisotropic radiation fields (Weingartner & Draine 2001b) should be also included. However, the approximation is not too crude: at the virial radius of a $z = 3$ galaxy of median mass (§ 4 and § 5), the gravitational and radiation pressure force (assuming a galactic mass-to-light ratio) on a $a=0.1\text{-}\mu\text{m}$ grain nearly compensate each other, being of order 10^{-23} dyne.

The drag force due to the IGM gas is of the same order (see Fig. 1) and dominates as the grain moves from its initial position, since the drag force on high velocity grains decreases less than the distance squared.

Grains in the IGM are charged, because of collisions with ions and because of the photoionization due to the metagalactic UV background. The charge influences both the drag and the sputtering efficiency. The charging processes we have considered and the typical charges of a grain in the IGM are described in § 3.2. We will denote with U the potential on the grain surface ($U = Ze/a$, where Z is the grain charge in units of the electric elementary positive charge e ; $Z = 694.5U[\text{Volt}][a[\mu\text{m}]]$). It is helpful to define the reduced potential

$$\phi = \frac{eU}{KT}.$$

Charged grains could be deviated from their path by the Lorentz force, if moving through a magnetic field. For simplicity we neglect this force here. If the primordial IGM magnetic fields are low as predicted in cosmological simulations ($B \approx 10^{-19} \text{ G}$; Gnedin et al. 2000), the Larmor radius would be of order 10 Gpc for the grain properties considered in this work (§ 3.2.3). Being this much larger than the typical length travelled by a grain in a Hubble time, the Lorentz force could indeed be neglected. Unfortunately, it is not clear if efficient large scale amplification mechanisms are present. Some observations seem to indicate intergalactic B-fields as high as 0.1 nG (Vallée 2004, and references therein), in which case charged grains would preferentially move along field lines. However, the inclusion of the Lorentz force is still prevented by the large uncertainties on the field direction, strength and structure.

The sputtering process is described in § 3.3. Because of collisions with gas particles, atoms may be knocked off a dust grain and released in the IGM. In a low temperature medium, the most relevant mechanism is *non-thermal* sputtering, in which the energy transferred to the grain's atoms is the kinetic energy of gas particles impacting at a supersonic grain speed v . Since we consider grains made of graphite and silicate (olivine), sputtering could be able to pollute the IGM with carbon, iron, magnesium, silicon and oxygen.

Finally, § 3.4 shortly describes how the physical prescription are implemented in our numerical code.

3.1 Drag Forces

A charged dust grain moving through a gas experiences a drag force due to the direct collision with the particles in the gas and to Coulomb interactions with the ions. Under the hypotheses that the collisions between grains and ions are elastic and that the grains are much smaller than the mean free path of the particles in the gas, we can follow Draine & Salpeter (1979) and write

$$F_{drag} = 2\pi a^2 KT \left\{ \sum_i n_i [G_0(s_i) + z_i^2 \phi^2 \ln(|\Lambda/z_i|) G_2(s_i)] \right\}, \quad (1)$$

where the summation is over the six kind of particles we have considered for the gas, z_i is the charge of each particle (in units of e ; $z_i = -1$ for electrons) and

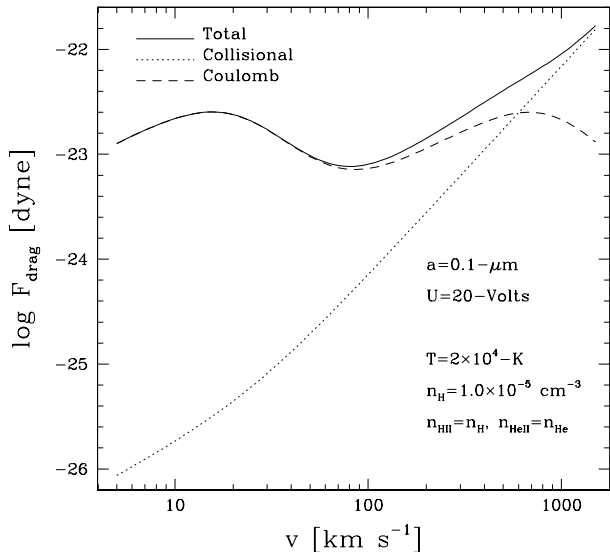


Figure 1. Drag force on a spherical dust grain of radius $a = 0.1\text{-}\mu\text{m}$ moving at velocity v through a gas with $T = 2 \times 10^4\text{-K}$ and $z = 3$ mean cosmic density. The gas is composed of H II, He II and electrons. The dotted lines is the force component due to collisional drag. The dashed line is the component due to Coulomb drag for a grain potential $U=20\text{-Volts}$. The solid lines represent the total drag.

$$\Lambda = \frac{3}{2ae\phi} \left(\frac{KT}{\pi n_e} \right)^{1/2}.$$

The first part of Eqn. (1) is the term due to the collisional drag (Baines, Williams & Asebiomo 1965), ignoring a negligible contribution due to Coulomb focusing. The second part describes the Coulomb drag (Spitzer 1962). For $G_0(s)$ and $G_2(s)$, whose exact formulae depend on the error function, we use the simple analytical approximations derived by Draine & Salpeter (1979),

$$G_0(s) \approx \frac{8s}{3\sqrt{\pi}} \left(1 + \frac{9\pi}{64}s^2 \right)^{1/2}, \quad G_2(s) \approx \frac{s}{\left(\frac{3}{4}\sqrt{\pi} + s^3 \right)},$$

which provide an accuracy within 1 and 10 per cent, respectively, for $0 < s < \infty$.

In Fig. 1 we show the drag force acting on a dust grain of radius $a=0.1\text{-}\mu\text{m}$ as it moves with velocity v through a gas of mean $z = 3$ cosmic density and $T = 2 \times 10^4\text{-K}$. We have assumed that the IGM is composed of H II, He II and electrons. If the grain is not charged (or the gas not ionised) only the collisional drag is present (dotted line). For a supersonic dust grain ($s_i \gg 1$) the collisional term in Eq. 1 reduces to (Shull 1978)

$$F_{\text{coll}} = \pi a^2 v^2 \sum_i n_i m_i. \quad (2)$$

As it can be seen in Fig. 1, the supersonic regime is reached at low velocities: for H and He we have $v \gg 18.1 \text{ km s}^{-1}$ and $v \gg 9.0 \text{ km s}^{-1}$, respectively (for the gas temperature adopted), and $F_{\text{coll}} \propto v^2$ beyond that velocity. At high velocities, collisions with helium ions constitute about 30 per cent of the collisional drag. Free electrons, instead, do not carry enough momentum to contribute more than a few percent to the drag force, at any velocity. Thus the collisional drag is nearly independent of the ionization state of the IGM.

For a charged grain moving through a plasma, one needs to consider also Coulomb drag. This is shown in Fig. 1 (dashed line) for a grain with a typical potential $U = 20\text{-Volts}$ (see § 3.2.3; the Coulomb drag does not depend on the sign of the grain charge). For small velocities, the Coulomb drag increases linearly with v . For supersonic velocities, instead, it decreases as v^{-2} . The first maximum at $v \approx 15 \text{ km s}^{-1}$ occurs when the dust grain has a velocity similar to the thermal velocity of H and He ($s_{\text{H}} \approx 1$ and $s_{\text{He}} \approx 1$). For larger v , the contribution of H and He to the Coulomb drag decreases until the electron component become dominant. A second local maximum is reached when $s_e = 1$ ($v \approx 680 \text{ km s}^{-1}$), after which the drag decreases again.

It is interesting to note that the Coulomb drag decreases with increasing gas temperature. This is because of the increasing number of gas particles moving faster than the grain, which do not contribute to the net drag (Northrop & Birmingham 1990). The collisional drag, instead, depends on \sqrt{T} for low velocity and is independent of T in the supersonic case.

3.2 Grain Charge

Dust grains immersed in a hot gas and subject to a UV background attain an electrical charge because of: i) collisions with electrons (which tend to make the charge more negative); ii) collisions with positive ions, and iii) photoejection of electrons from the grain by absorption of UV photons (which tend to make the charge more positive). If we denote with J_{ci} the charging rate due to collisions with ion i (i.e. the number of charges, in units of e , captured by a grain colliding with particle i per unit time) and with J_{pe} the rate for photoelectric charging, the grain charge at equilibrium can be found by imposing

$$J_{pe} + \sum_i J_{ci} = 0.$$

We ignore here charge quantization (Draine & Sutin 1987). This is a safe assumption for the large grains adopted in this work and for the large potentials they attain (see § 3.2.3).

3.2.1 Collisional Charging

We followed Shull (1978) to derive the charging rates on a spherical dust grain that moves relative to the gas. The charging rate due to collisions with particle i is²

$$J_{ci} = \pi a^2 n_i (z_i \xi_i + \delta_i) \left(\frac{KT}{2\pi m_i} \right)^{1/2} \frac{1}{s_i} \times \left\{ \sqrt{\pi} \left(\frac{1}{2} + s_i^2 - z_i \phi \right) [\text{erf}(s_i - s_o) + \text{erf}(s_i + s_o)] \right. \\ \left. + (s_i + s_o) \exp[-(s_i - s_o)^2] + (s_i - s_o) \exp[-(s_i + s_o)^2] \right\} \quad (3)$$

with erf the error function, ξ_i the sticking coefficient of the particle i , δ_i the secondary electron emission coefficient and

² Electrostatic polarization of a dust grain by the electric field of an approaching charged particle (Draine & Sutin 1987) is not included in Eqn. (3). Its effects are small for the typical charges described in § 3.2.3.

$$s_o = \begin{cases} 0 & z_i \phi < 0 \\ \sqrt{z_i \phi} & z_i \phi > 0 \end{cases}$$

the minimal atomic speed ratio for the approaching particle to win electrostatic repulsion. In the limit $s_i \rightarrow 0$, Eqn. (3) reduces to the classical result for a static grain (Spitzer 1978). If the grain moves relative to the gas, the frequency of collisions with ions and electrons is altered. For $s_i \gg 1$, Eqn. (3) tends to

$$J_{ci} = \pi a^2 n_i (z_i \xi_i - \delta_i) v (1 + \frac{1/2 - z_i \phi}{s_i^2}). \quad (4)$$

As for the sticking coefficients, we assume that half of the colliding electrons are captured by the grain ($\xi_e = 0.5$), the other half being scattered; and that all the ions will neutralise as they arrive on the surface, thus sharing their positive charge with the grain ($\xi_i = 1$; Draine 1978; Weingartner & Draine 2001c). For the coefficients for the secondary emission of electrons, δ_i , we used the empirical expressions given by Draine & Salpeter (1979). The coefficients depend on the energy of the impact, $\langle E_0 \rangle + m_i v^2/2$, where $\langle E_0 \rangle$ is the mean thermal energy of the impinging particle (Draine & Salpeter 1979). Because of the small sputtering rates (§ 3.3), we neglect the charge taken away from the grain by sputtered atoms (Draine & Salpeter 1979).

3.2.2 Photoelectric Charging

The photoelectric charging rate can be written as

$$J_{pe} = \pi a^2 \int_{\nu_{pet}}^{\nu_{max}} Q_{abs}(h\nu, a) Y(h\nu, a) \frac{4\pi J_\nu}{h\nu} d\nu, \quad (5)$$

where J_ν is the mean specific intensity of the UV background, $Q_{abs}(h\nu, a)$ is the absorption efficiency of a dust grain of radius a and $Y(h\nu, a)$ is the photoelectric yield, i.e. the probability that an electron is ejected when a photon absorption occurs. The lower limit of integration is the photoelectric threshold frequency, ν_{pet} , for which we use

$$\nu_{pet} = \begin{cases} W + eU & U \geq 0, \\ W & U < 0, \end{cases}$$

W being the workfunction, i.e. the ionization potential of a neutral bulk material. Thus, if the grain has negative charge, an electron is photoejected as soon as a photon with energy $h\nu > W$ is absorbed. If the grain has a positive charge, the photoejected electron needs to have a kinetic energy large enough to escape the attraction of the charged grain, therefore ionizing photons must have $h\nu > W + eU$. Weingartner & Draine (2001c) derive the photoelectric threshold for spherical grains taking into account geometric effects and polarization. They obtain values for ν_{pet} that differ from those used here by additional terms of order e^2/a and dependent on a^{-2} . For the large grains used in this work, those terms are negligible compared to W and we omit them here. We use $W = 8\text{-eV}$ and $W = 4.4\text{-eV}$ for graphite and silicates, respectively (Weingartner & Draine 2001c).

Following Weingartner & Draine (2001c), we write the photoelectric yield as

$$Y(h\nu, Z, a) = y_2(h\nu, a, Z) \min[y_0(\Theta) y_1(h\nu, a), 1],$$

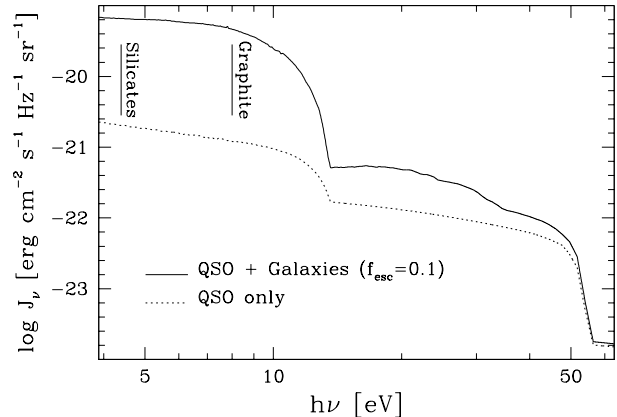


Figure 2. The $z=3$ UV background of Bianchi et al. (2001) including the contribution of galaxies and QSOs (solid line). The vertical bars show the workfunction adopted for silicates and graphite. The dotted line is the QSOs contribution to the background.

with y_0 the photoelectric yield of the bulk material and $\Theta = h\nu - W$. For graphite and silicates we use, respectively

$$y_0^{gra}(\Theta) = \frac{0.009(\Theta/W)^5}{1 + 0.037(\Theta/W)^5}, \quad y_0^{sil}(\Theta) = \frac{0.5(\Theta/W)}{1 + 5(\Theta/W)}.$$

In small particles, the photoelectric yield is enhanced with respect to bulk materials. For spherical grains of radius a , the enhancement factor is well approximated by

$$y_1(h\nu, a) = \left(\frac{\beta}{\alpha}\right)^2 \frac{\alpha^2 - 2\alpha + 2 - 2e^{-\alpha}}{\beta^2 - 2\beta + 2 - 2e^{-\beta}}$$

with $\beta = a/l_a$ and $\alpha = a/l_a + a/l_e$, l_a and l_e being the photon attenuation length and the electron escape length Draine (1978). We adopted $l_e = 10\text{\AA}$ (Weingartner & Draine 2001c). Using tabulated values for the optical properties of graphite and 'smoothed astronomical silicates'³ (Weingartner & Draine 2001a), we derived the photon attenuation length with $l_a = \lambda/[4\pi\text{Im}(m)]$, where λ is the radiation wavelength and $m(\lambda)$ the complex refractive index. A proper weighted mean has been used to take into account the anisotropy of graphite (Weingartner & Draine 2001c).

Laboratory measures on bulk materials have shown that the distribution of kinetic energy for photoejected electrons drop to zero at $E = 0$ and $E = h\nu - W$ and peaks at intermediate energies (Draine 1978). Weingartner & Draine (2001c) adopted a parabolic energy distribution and derived the probability for electron escape to infinity, y_2 . Again ignoring all terms of order e^2/a and dependent on a^{-2} , it is

$$y_2(h\nu, a, Z) = \begin{cases} (1 - \frac{eU}{h\nu-W})^2 (1 + \frac{2eU}{h\nu-W}) & U \geq 0, \\ 1 & U < 0. \end{cases}$$

Finally, we have used tabulated values of $Q_{abs}(h\nu, a)$ for spherical grains of graphite and 'smoothed astronomical silicates' (Weingartner & Draine 2001a). We did not consider photodetachment of electrons in the energy levels above the valence band of negatively charged grains (Weingartner & Draine 2001a), which can be ignored for the grain charges and radii considered here.

³ Available at <http://www.astro.princeton.edu/~draine>.

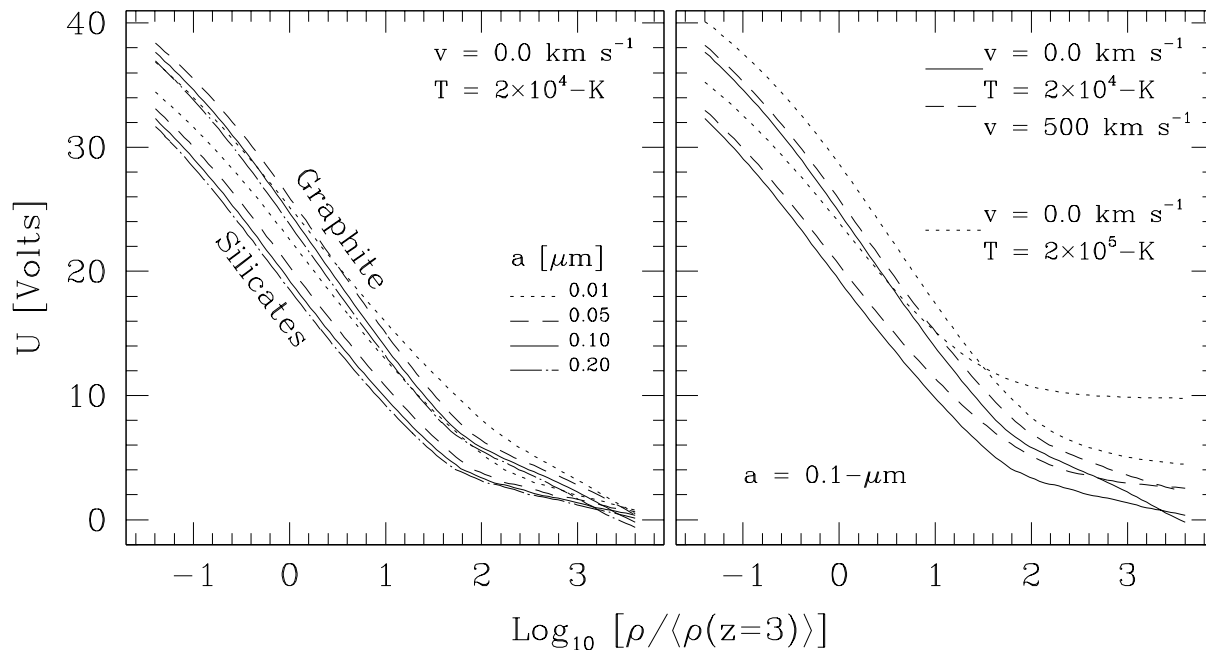


Figure 3. Equilibrium potentials for graphite and silicate dust grains exposed to the $z = 3$ UVB, as a function of the gas overdensity. In the left panel we show the equilibrium potentials for static ($v = 0$) grains of radii 0.01, 0.05, 0.1 and 0.2- μm (in both panels, the upper bundle of curves refers to graphite grains, the lower to silicates). We have assumed a gas made of H II, He II and electrons, with temperature $T = 2 \times 10^4\text{-K}$. In the right panel we show the effects of variation in grain velocity and gas temperature for a grain with radius $a = 0.1\text{-}\mu\text{m}$. For each grain material, the solid line refer to the same conditions as in the left panel, the dashed line to a grain moving with $v = 500\text{ km s}^{-1}$ in a $T = 2 \times 10^4\text{-K}$ gas, the dotted line to a static grain in a $T = 2 \times 10^5\text{-K}$ gas.

3.2.3 Typical grain charges in the IGM

We adopt in this work the ultraviolet background (UVB) of Bianchi, Cristiani & Kim (2001). The UVB, shown in Fig. 2, includes contributions from both QSOs and galaxies, assuming that a fraction $f_{\text{esc}} = 0.1$ of the H I-ionising UV light can escape internal absorption. For any observer's redshift, the UVB shows two breaks at frequencies $\nu > 13.6\text{-eV}$ and $\nu > 54.4\text{-eV}$ in the observer's rest frame, due to the absorptions of H I and He II Lyman continuum photons, respectively, from the residual neutral gas in the IGM. While the QSO contribution (dotted line) can be fitted between the breaks by a power law (mainly because of the assumption on the intrinsic QSO's spectrum), the H I-ionizing UVB including galaxies is only roughly described by $J_\nu \propto \nu^{-1.9}$ for $\nu < 54.4\text{-eV}$. The contribution to the photoelectric charging rates of frequencies $\nu > 54.4\text{-eV}$ is negligible, therefore we use $\nu_{\text{max}} = 54.4\text{-eV}$ in Eqn. (5). The UVB is computed integrating light coming from all objects up to a maximum redshift z_{max} . In Bianchi et al. (2001) we adopted $z_{\text{max}} = 5$. This assumption has no effect on H I-ionising photons: because of IGM absorption only local sources contribute to the calculation. For radiation at lower frequencies not able to ionise H I, the UVB depends on the redshift assumed for the first sources, mainly because of the nearly constant galaxy emissivity at $z > 2$ (Bianchi et al. 2001). However, as long as we use the UVB at $z < 4$, the photoemission rate in Eqn. (5) is only slightly affected by our choice for z_{max} .

In Fig. 3 we show the equilibrium potentials for graphite and silicate grains exposed to the $z = 3$ UVB, as a function of the gas overdensity. Again, the gas is composed of H II, He II and electrons and has $T = 2 \times 10^4\text{-K}$. In the left panel

equilibrium potentials are shown for static ($v = 0$) grains of radii 0.01, 0.05, 0.1 and 0.2- μm (spanning the range of radii relevant to this work). Because of the different photoelectric yields and absorption efficiencies, graphite grains generally attain a larger (more positive) potential than silicate grains.

In the low density IGM the grain potential reach a relatively high positive value (a few tens of Volts), in agreement with what found by Nath et al. (1999). The equilibrium potential is reached when the collisional charging rate for electrons J_{ce} is balanced by the photoelectric charging rate J_{pe} , the contribution of positively charged ions being greatly reduced by Coulomb repulsion ($J_{\text{ci}} \ll J_{\text{pe}}$). While the collisional charging rate depends on the particle density, the photoelectric charging does not. Thus, for low values of n_e , a high Coulomb attraction is needed to increase the collisional cross section, in order to have $J_{\text{ce}} \approx J_{\text{pe}}$. Charges for the grains studied here are always much lower than the maximum limit over which field emission of positive ions occurs (Draine & Salpeter 1979).

At higher density, the contribution of collisions to charging becomes progressively more important and the charge decreases. This partly explains why the slope of the equilibrium potential of a grain of given radius changes at higher densities (see Fig. 3). A second reason for this is that ν_{pet} goes across the Lyman discontinuity in the UVB. For very high densities, only collisional charging rates are important. Neglecting secondary emission, the classical result is recovered: grains have negative potential because of the higher collision rate of electron in a gas (Spitzer 1978; Osterbrock 1989). For the plasma composition and sticking

coefficients adopted here, the equilibrium would be reached for $\phi \approx -2.0$.

For a grain that moves at a supersonic speed, the collisional charging rate tends to Eqn. (4) and becomes larger than that in the static case. When $s_i \gg 1$ but still $s_e \ll 1$, J_{ci} gives a constant contribution to the positive charging rate, with a small dependence on the grain potential. When also $s_e \gg 1$, J_{ce} and J_{ci} almost compensate, apart from the contribution of gas particles impacting from directions normal to the grain motion, which results in a net negative charging rate proportional to ϕ/s_e^2 . Because of this, moving grains always have higher (more positive) equilibrium potentials. In Fig. 3 (right panel) we show the equilibrium potentials for a $a=0.1\text{-}\mu\text{m}$ grain moving in a $T = 2 \times 10^4\text{-K}$ gas at $v = 500 \text{ km s}^{-1}$. For the velocities explored in this work, differences with the static case are never larger than about 5-Volts.

In Fig. 3 (right panel) we also show the change in the equilibrium potentials of a $a=0.1\text{-}\mu\text{m}$ static grain when the temperature raises to $T = 2 \times 10^5\text{-K}$ gas. At higher temperatures gas particles move faster and the Coulomb cross section reduces. At low densities, a reduced J_{ce} has to compete with a J_{pe} unaltered by temperature changes and the equilibrium potential increases. According to the classical result, at high densities the charge would reach a high negative value. This is not the case when the secondary emission of electrons is included. The secondary emission of electrons decreases the negative charging rate due to electrons J_{ce} and increases the positive charging rates for ions J_{ci} . As a results, equilibrium potentials are higher when this process is included. The effect can be larger for higher temperatures (or for supersonic grains). In Fig. 3, the positive equilibrium potential attained in the high density gas for $T = 2 \times 10^5\text{-K}$ is due to secondary emission. If $\delta_e, \delta_i=0$, a static grain would have an equilibrium potential $U = -34.5\text{-Volts}$, while it is 4.2 and 9.8-Volts for graphite and silicates, respectively, when the secondary emission is accounted for (silicates have higher secondary emission for impinging electrons). Thus, secondary emission prevents dust grains in a hot overdense gas to reach high negative charges. The limiting negative potential below which field emission of electrons occurs (Weingartner & Draine 2001c) is never reached in this work. In the $T = 2 \times 10^4\text{-K}$ gas, secondary emission raises the equilibrium potential by less than a few Volts, and its effect can be mimicked by reducing the electron sticking coefficient to $\xi_e \approx 0.4$ (in most cases, the secondary emission due to colliding electrons is more important than that due to positively charged ions).

As the parameters describing the galactic contribution to the UVB (namely, the star formation history and the f_{esc} fraction) are quite uncertain, especially at high- z , we also computed charges when only the QSO contribution (dotted line in Fig. 2) is taken into account. Because of the reduced UV flux, the equilibrium charges are smaller in this case. However, the difference is small (a couple of Volts) and it does not modify significantly the results we present in the rest of the paper.

3.3 Grain Sputtering

The efficiency of the sputtering process is given by the sputtering yield, $Y_i(E, \theta)$, i.e. the number of atoms or molecules

of the target material that are sputtered in each collision with a projectile atom of material i . For each target/projectile combination, the sputtering yield depends on the impact energy E and on the angle θ (relative to the surface normal; $\theta = 0$ for normal impact) of the impacting particle. Our targets are dust grains made of graphite or silicates, while we will consider neutral and ionised hydrogen and helium atoms as projectiles. The sputtering yield does not depend explicitly on the charge of the projectile (ions rapidly neutralise when approaching a solid surface; § 3.2.1), although the energy of the impact E depends on Coulomb repulsion/attraction.

From Y_i we can derive the sputtering rate, i.e. the number of atoms that are sputtered off each grain per unit time, dN/dt . For a charged (non-rotating) spherical dust grain of radius a that moves with velocity v through a Maxwellian gas, we can write (Draine & Salpeter 1979)

$$\frac{dN}{dt} = \pi a^2 v \sum_i n_i \int_{\epsilon_{\min}}^{\infty} g_i(\epsilon, \phi) \langle Y_i[E = (\epsilon - z_i \phi)KT] \rangle_{\theta} d\epsilon, \quad (6)$$

where again the summation is over all relevant projectile particles of species i , $\epsilon_{\min} = \max[0, z_i \phi]$ and $\langle Y_i(E) \rangle_{\theta}$ is the angle averaged sputtering yield, given by

$$\langle Y_i(E) \rangle_{\theta} = 2 \int_0^{\pi/2} Y_i(E, \theta) \sin \theta \cos \theta d\theta. \quad (7)$$

The function g_i is given by

$$g_i(\epsilon, \phi) = \frac{\exp(-s_i^2 - \epsilon)}{s_i^2} \sqrt{\frac{\epsilon}{\pi}} \left(1 - \frac{z_i \phi}{\epsilon}\right) \sinh(2\sqrt{\epsilon} s_i).$$

For supersonic grains ($s_i \rightarrow \infty$) the function g_i tends to

$$g_i(\epsilon, \phi) = \left(1 - \frac{z_i \phi}{\epsilon}\right) \delta(\epsilon - s_i^2)$$

and the rate for *non-thermal* sputtering is obtained,

$$\frac{dN}{dt} = \pi a^2 v \sum_i n_i \left(1 - \frac{2z_i eU}{m_i v^2}\right) \langle Y_i[\frac{1}{2}m_i v^2 - z_i eU] \rangle_{\theta}, \quad (8)$$

where the term within round brackets is a correction to the grain cross section due to Coulomb focusing (Spitzer 1978).

A few analytical models for the sputtering yield of astronomical dust materials can be found in the literature (Draine & Salpeter 1979; Tielens et al. 1994). As a comparison, we refer here to the sputtering yields of Draine & Salpeter (1979) for graphite and for olivine (a typical silicate, FeMgSiO_4 ; Draine 1995). Normal incidence sputtering yields are shown in Fig. 4, together with a few experimental results which are taken from Draine (1995). Above a certain threshold energy, the yield increases steeply, reach a maximum and then decreases slowly for higher impact energies. The normalization of $Y_i(E, \theta = 0^\circ)$ was chosen to fit the available data. Because of the lack of experimental data for low impact energies, which is the most important in astrophysical applications, the sputtering yield in proximity of the threshold is poorly constrained. The dependence on the collision angle is uncertain as well, and it is usually assumed that $Y_i(E, \theta) \sim 1/\cos \theta$. Under this assumption, it follows from Eqn. (7) that the angle averaged sputtering yield is twice the normal one.

Field et al. (1997) and May et al. (2000; see also Flower et al. 1996; Jurac et al. 1998) derived sputtering

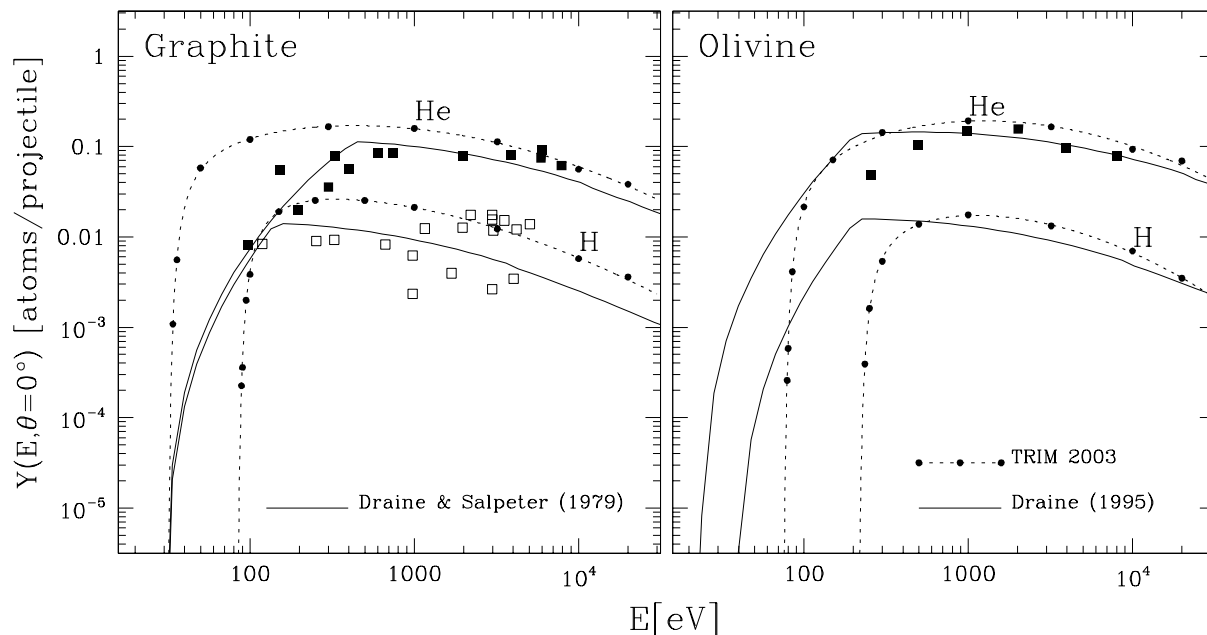


Figure 4. Normal incidence ($\theta = 0^\circ$) sputtering yields for H and He on graphite and silicates (olivine), as a function of the impact energy. Solid curves are theoretical estimates from Draine & Salpeter (1979, graphite) and Draine (1995, olivine). Small dots are our results using the TRIM 2003 code, together with the fits of Eq. (9) (dotted lines; see text for details). Squares are experimental measures from Draine (1995): closed symbols are for He, open symbols for H. As there are no measures for sputtering on silicates, datapoints in the right panel are for a similar material, Si O₂ (Draine 1995).

yields using the Monte Carlo code for the TRansport of Ions in Matter (TRIM; Ziegler et al. 1985). Briefly, TRIM simulates the bombardment of a plane-parallel target by projectiles of given kinetic energy and impact angle with respect to the surface. The target is simulated as amorphous (i.e. given the density ρ , the position of each atom inside the target is random). The depth inside the material at which the projectile hits a target atom is derived from interatomic potentials dependent on the colliding elements. If an atom in the target is given an energy larger than the Displacement Energy E_D , it will be able to escape from its position (the lattice site) and it will lose to the lattice an amount of energy given by E_B , the Bulk Binding Energy. Recoiling atoms may collide themselves with other target atoms. TRIM follows the whole collision cascade. Finally, an atom in the proximity of the target surface is counted as sputtered if the component of its kinetic energy normal to the surface is larger than the Surface Binding Energy, E_S . Several projectiles are needed to derive a mean sputtering yield. In order to have an estimate alternative to the widely used Draine & Salpeter (1979) yields, we have used the 2003 version of TRIM⁴ to derive the sputtering yield for graphite ($\rho=2.266$ g cm⁻³, $E_D = 25$ eV, $E_B = 3.0$ eV, $E_S = 7.41$ eV; Field et al. 1997) and olivine ($\rho=3.843$ g cm⁻³, $E_D = 50$ eV, $E_B = 9.7$ eV, $E_S = 5.64$ eV; May et al. 2000).

We ran TRIM to have $Y_i(E, \theta)$ for several values of E and θ . Our results for sputtering of olivine by He are very similar to those published by May et al. (2000). The sputtering yields we obtain for He into graphite are at least a fac-

tor of two larger than those reported by Field et al. (1997), probably because they used an earlier version of the code. None of those author gives sputtering yields with H as a projectile. In Fig. 4 we show the sputtering yields for $\theta = 0^\circ$. Above a certain threshold energy, yields increase steeply, reach a maximum and decrease at a slower rate for higher energies (because projectiles implant deeper into the target). At high energies, the behavior of the TRIM results is similar to the analytical models of Draine & Salpeter (1979), although graphite yields for both H and He are higher than the laboratory results. In the proximity of the threshold, differences are larger. In general, the threshold energies of the analytical yields are lower than those derived with TRIM (with the exception of He into graphite). Such discrepancies may be the result of uncertainties in the estimate of the energy parameters (E_D , E_B and E_S) adopted in the TRIM calculations, as discussed by Field et al. (1997). In particular, we found that a variation of 20 per cent in E_S causes a variation of about 30 per cent in the sputtering yield at high energies, while the region of the threshold depends more on the choice of E_D : by varying E_D of 20 per cent the threshold energy changes by 25 per cent. We stress again the uncertainty in the derivation of the yield in the proximity of the threshold: the cross sections used by TRIM in computing the collisions at low energies are based on extrapolations from experimental data which are only available at higher energies.

The behavior of the sputtering yield for $\theta > 0^\circ$ depends on the energy E . For high E values, the yield increases with θ faster than the usually assumed $1/\cos\theta$ dependence, while at energies lower than the energy corresponding to the maximum yield, $Y_i(E, \theta)$ is flatter and decreases when the projectile approaches grazing incidence.

⁴ The TRIM program is part of the SRIM package, which can be downloaded at <http://www.srim.org>.

Table 1. Best-fit parameters to be used in Eq. 9 to calculate the angle-averaged sputtering yields of H and He on graphite and olivine. For olivine, parameters are given for each atomic species in the compound and for the total number of sputtered atoms. The parameters in the left panel refer to $\langle Y_i(E) \rangle_\theta$ as defined in Eq. (7) (the *streaming yield* adopted in this work). For completeness, in the right panel we also give the parameters derived using Eq. (10) to define the mean (the *isotropic yield*, preferred by Field et al. 1997 and May et al. 2000).

Streaming Yield					Isotropic Yield					
k	β	γ	E_{th}	E_{max}	k	β	γ	E_{th}	E_{max}	
	(eV)		(eV)	(eV)		(eV)		(eV)	(eV)	
H → Graphite										
4.356E-2	3.997E+1	1.059E-1	8.133E+1	3.620E+2	6.322E-2	4.176E+1	1.165E-1	8.119E+1	1.049E+3	
He → Graphite										
3.301E-1	1.456E+1	1.249E-1	3.075E+1	1.095E+3	5.140E-1	1.518E+1	1.231E-1	3.072E+1	2.175E+3	
H → Olivine										
5.029E-3	1.486E+2	1.423E-1	2.011E+2	1.329E+3	Fe	7.726E-3	1.480E+2	1.457E-1	2.020E+2	2.965E+3
4.778E-3	1.386E+2	1.455E-1	2.033E+2	1.198E+3	Mg	7.390E-3	1.544E+2	1.466E-1	2.007E+2	2.403E+3
4.441E-3	1.078E+2	1.728E-1	2.094E+2	1.552E+3	Si	7.020E-3	1.306E+2	1.569E-1	2.057E+2	2.739E+3
1.789E-2	1.044E+2	1.588E-1	2.073E+2	1.469E+3	O	2.842E-2	1.210E+2	1.477E-1	2.053E+2	2.537E+3
3.207E-2	1.140E+2	1.584E-1	2.063E+2	1.444E+3	Tot	5.048E-2	1.301E+2	1.482E-1	2.042E+2	2.609E+3
He → Olivine										
5.361E-2	5.502E+1	1.276E-1	7.056E+1	2.018E+3	Fe	7.819E-2	5.993E+1	1.174E-1	6.994E+1	4.106E+3
4.805E-2	6.232E+1	1.173E-1	6.962E+1	1.630E+3	Mg	6.816E-2	7.180E+1	1.036E-1	6.851E+1	3.093E+3
4.794E-2	5.780E+1	1.223E-1	7.056E+1	1.748E+3	Si	6.991E-2	6.353E+1	1.166E-1	6.988E+1	3.336E+3
1.893E-1	4.489E+1	1.294E-1	7.101E+1	1.873E+3	O	2.741E-1	4.774E+1	1.193E-1	7.076E+1	3.373E+3
3.388E-1	4.970E+1	1.276E-1	7.066E+1	1.863E+3	Tot	4.910E-1	5.316E+1	1.186E-1	7.028E+1	3.458E+3

As a result, $\langle Y_i(E) \rangle_\theta > 2Y_i(E, \theta = 0^\circ)$ at high energies and $\langle Y_i(E) \rangle_\theta \approx Y_i(E, \theta = 0^\circ)$ close to the threshold (see also the discussion in Jurac et al. 1998). TRIM calculations are made using a plane-parallel infinite target. Sputtering yields may increase for spherical grains of the dimension of the mean penetration depth of a projectile (Jurac et al. 1998). As we mainly deal with large grains, we do not consider this radius-dependent enhancement.

The data points computed with TRIM were fitted with the following function:

$$Y(E) = k \exp \left[-\frac{\beta}{E - E_{\text{th}}} - \gamma \left(\ln \frac{E}{E_{\text{max}}} \right)^2 \right]. \quad (9)$$

While the first term in Eqn. (9) (introduced by May et al. 2000) well describes the rapid increase of the sputtering yield in the proximity of the threshold energy E_{th} , the second term, centered on the energy value E_{max} , is needed to reproduce the maximum and the slow decrease of $Y(E)$ at higher energies. The function provides a remarkably good description of both $Y_i(E, \theta)$ (see, for example the TRIM data points for $Y(E, \theta = 0^\circ)$ and their fit in Fig. 4) and the angle averaged yield $\langle Y_i(E) \rangle_\theta$ of Eqn. (7), with most of the data points (~ 95 per cent) being within less than 10 per cent of the fitted function. The best-fit values of E_{th} , E_{max} and the parameters k , β and γ can be found in Table 1 (right panel)⁵. For olivine, sputtering yields are slightly different for each of the elements in the compound. For simplicity, we

use here the sputtering yield for the total number of atoms. Parameters for the fit of the total sputtering yield of olivine are also given in Table 1.

To show the differences between the analytical and the TRIM sputtering yields, we plot in Fig. 5 (right panel) the sputtering rates computed from Eqn. (6) for a graphite or olivine grain moving through a gas composed of H II, He II and electrons. The grain has radius $a = 0.1\text{-}\mu\text{m}$ and equilibrium potential $U = 20\text{-eV}$. The gas has mean $z = 3$ cosmic density and temperature $T = 2 \times 10^4\text{-K}$. For both analytical and TRIM sputtering yields, the low velocity sputtering rate is obviously dominated by collisions with the more massive He atoms. The contribution of the more abundant H atoms becomes important for $v > 100 - 200 \text{ km s}^{-1}$ (where both He and H sputtering yields depend weakly on the impact energy). As said for the normal incidence case, the largest differences between TRIM and analytical sputtering rates are for graphite grains. However, the difference is small and the results shown in this paper do not change significantly when one of the yields is preferred over the other (see § 4). For the mean conditions considered in this work,

of projectiles it is more appropriate to use the *isotropic yield*, given by

$$\langle Y_i(E) \rangle_\theta = \int_0^{\pi/2} Y_i(E, \theta) \sin \theta d\theta. \quad (10)$$

While Field et al. (1997) and May et al. (2000) prefer the latter, we use in this work the former. As they pointed out, differences between the two means are not large. For completeness, we also give the best fit parameters for the *isotropic yield* in the right panel of Table 1.

⁵ The angle-averaged yield of Eq. (7) is referred to in Field et al. (1997) and May et al. (2000) as the *streaming yield*, appropriate for projectiles which streams in one dimension and collides with a non-rotating spherical grain. However, for a isotropic distribution

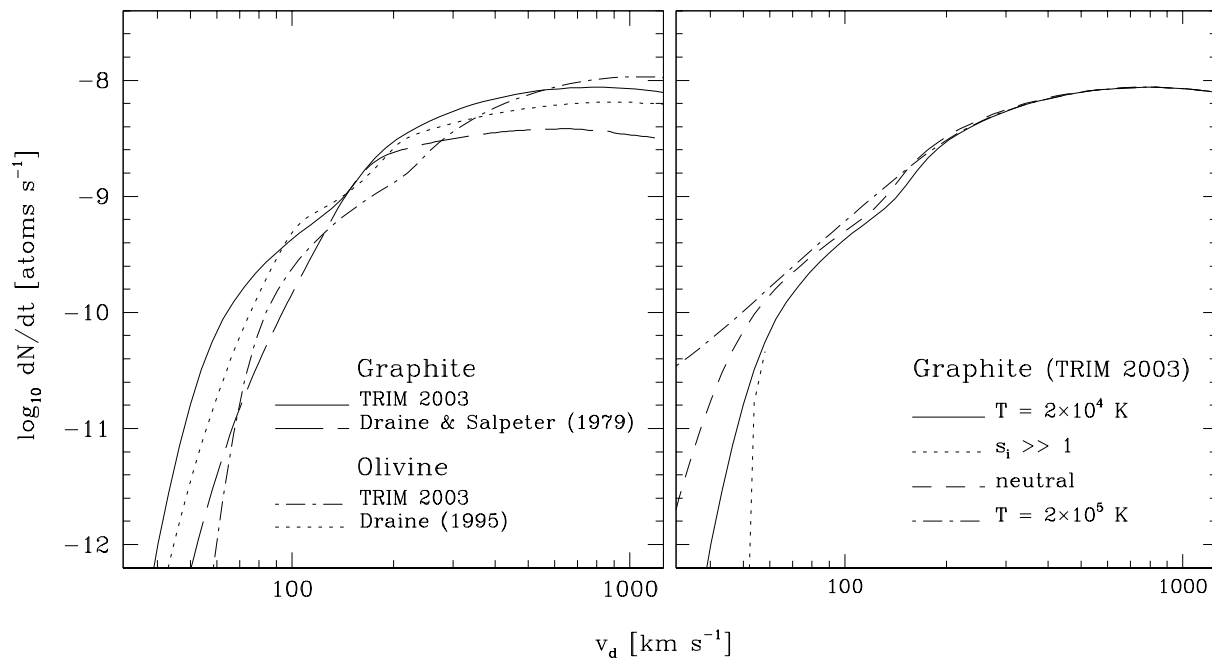


Figure 5. Sputtering rates for a graphite and olivine grain of radius $a = 0.1\text{-}\mu\text{m}$, moving with velocity v through a gas with mean $z = 3$ cosmic density. The gas is assumed to be composed of H II , He II and electrons. In the left panel the sputtering rates are shown for the TRIM results (graphite- solid line, olivine- dotted-dashed line) and for the analytical model (graphite- dashed line, Draine & Salpeter 1979; olivine- dotted line, Draine 1995), for a mean gas temperature $T = 2 \times 10^4\text{-K}$ and a grain equilibrium potential $U=20\text{-Volts}$. In the right panel we show the TRIM 2003 sputtering rate for graphite under different conditions. Solid line: same as in the left panel; dotted line: supersonic approximation (Eq. 8); dashed line: neutral grain (or/and neutral gas); dotted-dashed line: $U=20\text{-Volts}$ charged grain moving in a $T = 2 \times 10^5\text{-K}$ gas.

sputtering is mostly due to the grain motion (*non thermal* sputtering), as it can be seen in the right panel of Fig. 5: for $v \gtrsim 100 \text{ km s}^{-1}$, the supersonic approximation (dotted line) is very close to the full calculation (solid line). In most cases, the grain potential acts to increase the effective sputtering threshold, because part of the impact energy has to be spent in overcoming the Coulomb repulsion between the positively charged grain and the ions acting as projectiles. This is shown by the higher sputtering rate for a neutral grain for $v \approx 100 \text{ km s}^{-1}$ (left panel: dashed line). If the gas temperature increases (left panel: dot-dashed line) the contribution of thermal sputtering becomes dominant for low velocities.

3.4 Implementation

The motion of dust grains is studied in a three-dimensional grid (typically made of 128^3 cells). For each cell in the grid, gas density, temperature and ionization state are defined. After the determination of the position of the galaxies in the computational volume grid, grains are ejected into the IGM over the whole solid angle (from the center of each galaxy). The motion is assumed to start at a distance from the galaxy equal to its virial radius. A single ejected grain is thus characterised by its composition (graphite or olivine), radius a , velocity v and path direction. All these initial quantities are derived randomly with a Monte Carlo procedure from the adopted distribution (usually, those defined in § 2). Along the path the grain crosses cells with different gas conditions and its properties (velocity, charge and radius) change.

As the grain enters a cell, it is instantaneously assigned an equilibrium potential (the time necessary to reach the equilibrium, $t \approx |Z/J_{ce}|$ is usually much shorter than the time necessary for a grain to go across a cell; for the mean dust and gas conditions considered here, $t \approx 25$ yrs). For a fixed UVB, the equilibrium potential will depend on the gas density, temperature and plasma composition and on the grain material, radius and velocity. Given the equilibrium potential and the other gas and dust properties, we can compute the sputtering rate appropriate for the cell, dN/dt . The total number of atoms that are released as the grain moves through the cell is then $\Delta N = (dN/dt)(\Delta l/v)$, where Δl is the length of the grain path inside a cell. These sputtered atoms are deposited in the cell. As a result of sputtering, the grain loses mass (its radius reduces).

Finally, we compute the reduction in velocity, $\Delta v = -(\Delta l/v)F_{\text{drag}}$, due to collisional and Coulomb drag. The grain velocity (and radius) is updated when the grain leaves a cell and enters the next along the path. The process is then repeated (computation of equilibrium charge, of deposited atoms and reduction in velocity) and the grain motion followed for the chosen time duration of the simulation t_f (unless the velocity is so small that the grain will not move more than one cell in the remaining time). If Δv is large in a cell the grain path is split in smaller units and Δv , charge and ΔN are computed for each of them. We found that assuming $|\Delta v|/v < 0.1$ for each path segments provides accurate results without overly increasing the computational time. For the cosmological simulation of § 5, path splitting is typically required at the end of a grain's path, for velocities below 100

km s⁻¹ (the simulations of § 4 are computed with a larger spatial resolution).

In practice, the Monte Carlo procedure is run for N_p cycles (or grain *packets*) to assure a good statistics (i.e. sampling of initial grain properties and path directions). If N_g is the total number of grains that are ejected into the IGM in a simulation (defined by the mass of ejected dust and the size distribution), in each cycle $N_c = N_g/N_p$ identical grains will be ejected along a chosen direction. Thus, for each cell, $N_c \times \Delta N$ atoms are deposited in the IGM. The final output of the simulation is a grid with the number density of sputtered atoms. The final positions of the dust grains along their path is also stored.

4 RESULTS: HOMOGENEOUS DENSITY

To understand the details of grains motion and sputtering, we first analyze the case of a single galaxy ejecting grains into a homogeneous medium with $z=3$ mean cosmic density. The IGM is assumed to be composed of H II, He II and electrons. Unless it is said otherwise, the gas temperature is assumed to be $T = 2 \times 10^4$ -K and the TRIM 2003 sputtering yield are used in the calculations. As we said in § 3.4, we study the motion of the grain from the virial radius R_V , defined as the radius of the sphere enclosing a mean density of 200 times the critical density (Navarro et al. 1997). In the cosmological simulation described in the next section, a galaxy of *median* mass has a dark matter halo of $1.5 \times 10^{10} M_\odot$ (and a baryonic content of $1.5 \times 10^9 M_\odot$); the appropriate value for the virial radius is $R_V = 20$ kpc (proper units). We follow the motion of each grain for $t_f=1$ Gyr: the results of the simulation can thus be compared to the observed properties of the universe at $z = 2$. During this time stretch, the UVB flux increases only by 25 per cent (Bianchi et al. 2001); we neglect this time dependency in the calculations.

It is instructive to study the velocity evolution of dust grains of different size and material. In Fig. 6 we show v as a function of the distance R from the center of the galaxy. Grains are ejected at R_V with three different initial velocities $v_0 = 100, 500$ and 1000 km sec⁻¹. The two top panels refer to the case of grains of radius $a=0.1$ - μm , while in the two bottom panels $a=0.01$ - μm . Panels to the left are for graphite grains, those on the right for olivine. With the dashed line we show the results obtained for a grain whose charge is kept neutral (i.e. only the collisional part is included in the drag force). For the same initial velocity, larger grains can attain larger distances from the galaxy: despite having larger cross sections when colliding with the IGM atoms, their deceleration is smaller because they are heavier. For the same reason, heavier olivine grains travels to larger distances R . This dependence on the grain size and grain material density can be derived analytically for a neutral grain of radius a moving at supersonic speed. By integrating Eqn. 2 and 8 and neglecting the erosion of the grain due to sputtering (the radius a is kept constant), the velocity of the grain as a function of the distance R from the center of the galaxy can be written as

$$v(R > R_V) = v_0 \exp \left[-\frac{3(R - R_V)}{4a\rho} \sum_i n_i m_i \right]. \quad (11)$$

The supersonic approximation for neutral grains of Eqn. 11 is shown as a dotted line in Fig. 6 (for ease of presentation, only for $v_0=1000$ km sec⁻¹). The difference between the approximation and the curve for the case with only collisional drag is due to grain erosion. Despite small grains have smaller sputtering rates (see Eqn. 6) they contain less atoms and their size reduces more. For $v_0=1000$ km sec⁻¹, $a=0.01$ - μm grains lose in the IGM approximately 3×10^5 atoms, reducing their radius by 30-40 per cent (graphite and olivine, respectively). Conversely, $a=0.1$ - μm grains lose 2×10^8 atoms but their radius reduces less, by 20-25 per cent.

The results for the complete calculation including grain charge and Coulomb drag is shown in Fig. 6 by the solid lines. When exposed to the $z=3$ UVB, 0.1 - μm graphite grains attain a potential of about 25-Volts, while the potential of olivine grains is about 20-Volts (the exact value depending on the grain velocity; § 3.2.1). Because of Coulomb drag, the maximum distance R to which a grain can travel in the time t_f is reduced. Having a smaller charge (together with the larger mass), high velocity olivine grains can still travel at considerable distances (400-500 kpc) from the galaxy with velocities (kinetic energies) above the threshold for significant sputtering. Instead, high velocity graphite grains eventually stop at $R \lesssim 300$ kpc. Grains with $a=0.01$ - μm attains potentials a couple of Volts larger than those with $a=0.1$ - μm . As even in the neutral case small grains were not able to go beyond $R \approx 200$ kpc, when the Coulomb drag is included they stop within 50 kpc from the ejection, even for the less restrictive case of a $v_0=1000$ km s⁻¹ olivine grain. Small grains do not travel out to significant distances in the IGM. An analogous result has been obtained for the dust ejection from galaxies by some of the authors listed in § 2, although with a more detailed study of the grain motion, including gravitation and radiation pressure. This is why from now on we will use, as described in § 2, a flat size distribution, with $0.05 < a[\mu\text{m}] < 0.2$, suggested by literature models. Together with this we will assume a flat distribution of initial velocities, within the range $100 < v < 1000$ km s⁻¹.

Fig. 7 displays the carbon and silicon IGM metallicities⁶ resulting from the sputtering of carbon and silicon⁷ atoms off graphite (left panel) and olivine grains (right panel), for the adopted size and velocity distributions. The metallicity is reported as a function of the distance from the galaxy, R . The metallicity levels produced in our simulations depend linearly on the number of grains N_g ejected (equivalent to the ejected dust mass, for a fixed size distribution). The mass of dust ejected in Fig. 7 has been derived from the baryonic mass of our *median* $z = 3$ galaxy, by assuming

⁶ The metallicity of element X is given by $[X/H] = \log(n_X/n_H) - \log(n_X/n_H)_\odot$, where n_X is the number density of element X and $(X/H)_\odot = \log(n_X/n_H)_\odot$ is the solar abundance. We use $(C/H)_\odot = -3.44$ and $(Si/H)_\odot = -4.45$ (Anders & Grevesse 1989).

⁷ As described in § 3.3, we have used the yield for the total number of atoms sputtered off olivine. The number density of Si (and Fe, Mg) is thus 1/7 the total number density of atoms released by olivine grains in the IGM (the O number density being four times higher). The use of the rescaled total sputtering yield provides a good approximation to the specific sputtering yields for each of the species composing the material.

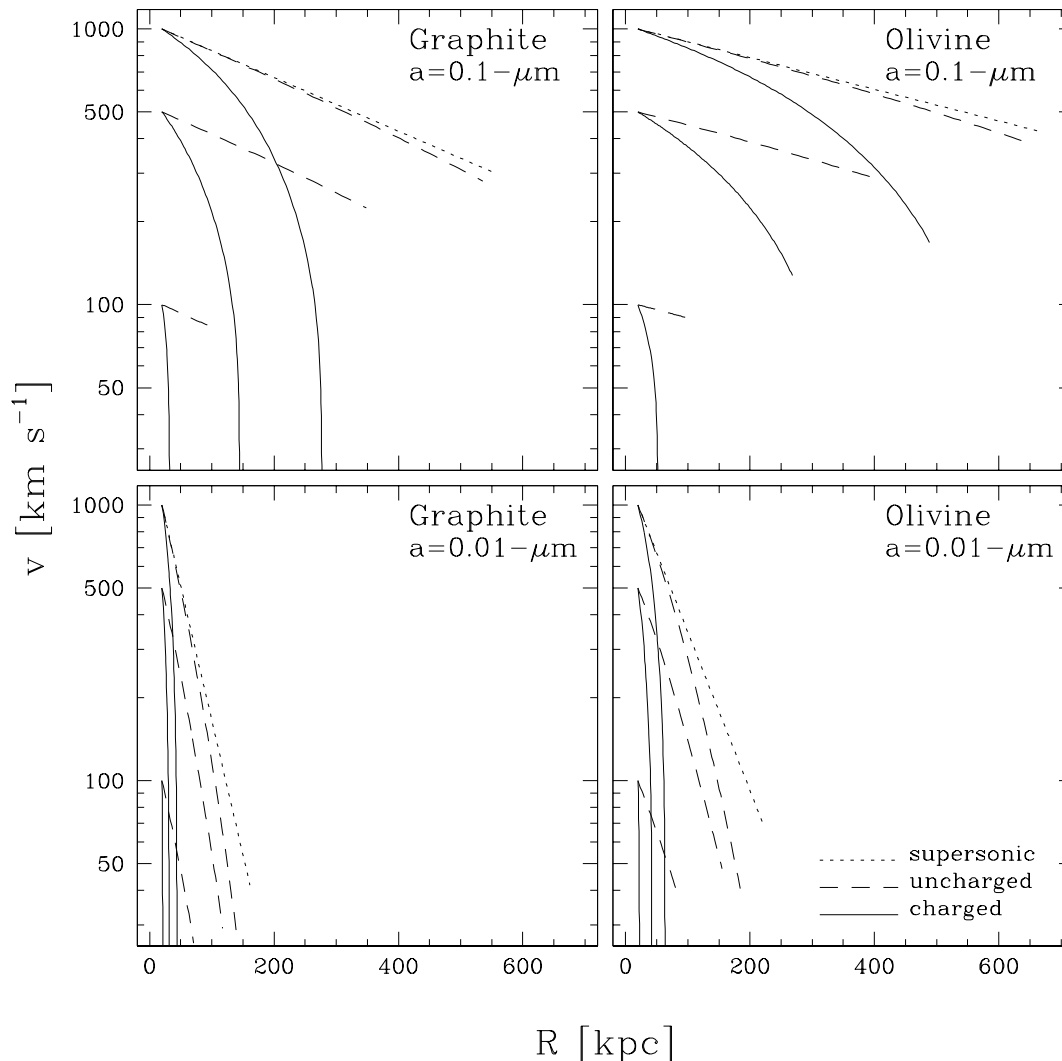


Figure 6. Velocity of dust grains injected into a homogeneous medium with mean $z = 3$ cosmic density, as a function of the distance from the source galaxy, R . For each panel, we show the velocity change of three grains with initial velocities (at $R_V = 20$ kpc) $v_0 = 100$, 500 and 1000 km s^{-1} (from bottom to top). The two upper panels show the velocity of graphite (left) and olivine (right) grains of radius $a = 0.1\text{-}\mu\text{m}$. The two lower panels show the same, but for $a = 0.01\text{-}\mu\text{m}$. Solid lines show the results when the whole physics described in § 3 is taken into account, while dashed lines refer to the case in which the grain charge has been set to zero. For the $v_0 = 1000$ km s^{-1} we also show the solution for the neutral supersonic approximation of grains with a fixed radius (Eqn. 11). The gas is made of H II, He II and electrons and has $T = 2 \times 10^4\text{-K}$. The TRIM 2003 sputtering yields have been used (§ 3.3).

that, at maximum, 1/500 of the baryonic mass is in dust in a galaxy (Edmunds & Eales 1998) and that 10 per cent of the total dust mass can reach the IGM (see Sect. 2). In total, $3 \times 10^5 M_\odot$ of dust (both graphite and silicate) are ejected into the IGM for the simulation of Fig. 7. Though we believe this to be a reasonable upper limit, the metallicity results can be easily scaled for any desired ejected mass of dust.

We compare the results of our simulation with the metallicities of C and Si derived by Schaye et al. (2003) and Aguirre et al. (2004). They analyzed the pixel optical depth in a set of high resolution observations of the Ly α forest using numerically simulated spectra and estimated the metallicity as a function of redshift and gas density. The gray areas in Fig. 7 show the median metallicity ($\pm 1\sigma$ of lognormal scatter) for gas of mean density (overdensity $\delta = 1$) at $z = 2$. The [Si/H] value has been extrapolated

from the ratio [Si/C] (Aguirre et al. 2004), with the caveat that it has been derived only for gas with $\delta > 3$. The scatter plotted for [Si/H] is that derived for [C/H]. Schaye et al. (2003) find no significant trend for [C/H] versus redshift in the range $1.8 < z < 4.1$. A detailed study of the metal enrichment history is needed to assess whether this lack of evolution can be explained by dust sputtering or galactic winds (Aguirre et al. 2001c), or if instead an early enrichment from pre-galactic ($z \approx 9$) sources is necessary (Madau et al. 2001). Here, we simply want to check if it is possible to reproduce, by using the dust sputtering mechanism only, the same level for [C/H] and [Si/H] as inferred from observations.

Fig. 7 shows that it is possible to obtain metallicity levels similar to those inferred from observations, at least for distances from the galaxy of $R \lesssim 200$ kpc. Within this range,

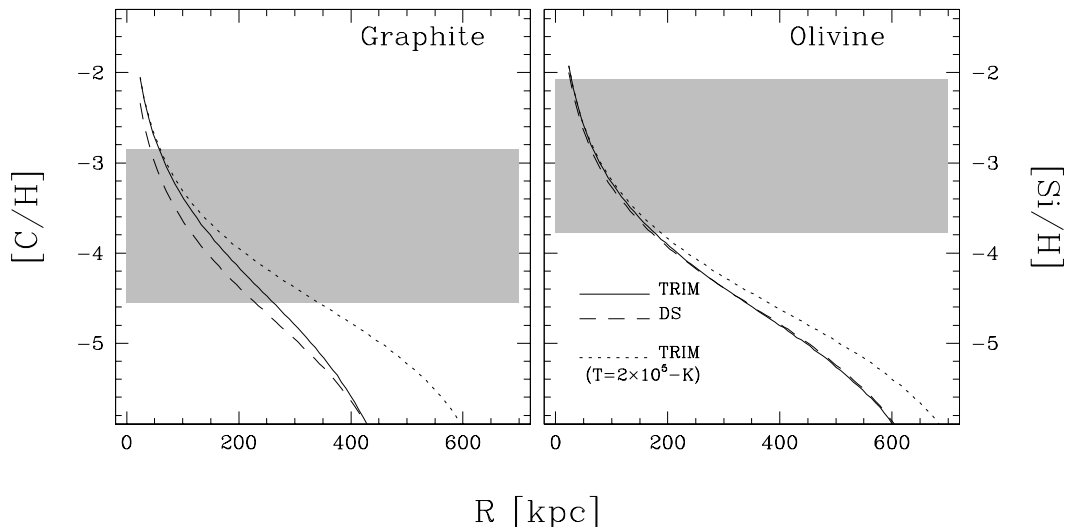


Figure 7. IGM metal pollution due to dust grains injected into a homogeneous medium with mean $z = 3$ cosmic density, as a function of the distance from the source galaxy, R . The left panels show the carbon metallicity $[C/H]$ resulting from erosion of graphite grains, while the right panels show the silicon metallicity $[Si/H]$ resulting from erosion of olivine grains. For each material, a flat distribution in the range $0.05 < a [\mu\text{m}] < 0.2$ has been used for the grain radii and a flat distribution in the range $100 < v_0 [\text{km s}^{-1}] < 1000$ for the grain initial velocities. The gas is made of H II , He II and electrons and has $T = 2 \times 10^4$ -K. In total, $3 \times 10^5 M_\odot$ of dust has been ejected. The results shown with solid lines have been obtained using the TRIM 2003 sputtering yields, while for the dashed lines the Draine & Salpeter’s yields have been used. The dotted lines refer to the TRIM 2003 case, but the gas temperature has been raised to 2×10^5 -K. The gray areas show the metallicities derived at $z = 2$ for the overdensity $\delta = 1$ (Schaye et al. 2003; Aguirre et al. 2004).

the metallicity levels are quite similar for both materials. As we saw in Fig. 6 olivine grains can travel to larger distances and pollute with metals a larger area. However, the difference in the trend can be appreciated only at $R \gtrsim 300$ kpc, where grains have reduced velocities and thus produce low levels of metallicity. We remind the reader that we have assumed, as an upper limit, the same relative abundance of graphite and silicate grains in the ejected dust. If silicates have a smaller ejection efficiency, as some studies suggest (see Sect. 2) the metallicity level in Fig. 7 will be lower (but the spatial distribution will be the same).

A change in the gas temperature does not affect significantly the results. The dotted curve shows the case for $T = 2 \times 10^5$ -K. The metallicity becomes higher only for larger R , due to grains that are not supersonic anymore (see, e.g., the analogous case in Fig. 5). Again, since graphite grains are slowed down more than those made of olivine, the difference is higher for $[C/H]$ than for $[Si/H]$. Because the sputtering yield is quite flat for high energies, a further increase in the gas temperature does not produce a dramatic change in the results. Even for an extreme case in which $T = 2 \times 10^7$ -K, the metallicities are only about 0.3-0.4 dex higher than those for $T = 2 \times 10^4$ -K. In Fig. 7 we also show the results when the traditional Draine & Salpeter sputtering yields are used (dashed lines). The differences are small, especially when compared to the large uncertainties and scatter of the metallicities inferred from observations. Graphite grains produce a lower $[C/H]$ (but by only 0.2 dex) when using Draine & Salpeter yields, while the difference is smaller for olivine. This is mainly due by the difference in sputtering rates for $v > 200 \text{ km s}^{-1}$, which is larger for graphite than for olivine (see the left panel of Fig. 5). For the rest of the paper, we will use the TRIM 2003 sputtering yields.

5 RESULTS: COSMOLOGICAL SIMULATION

We now study the motion of grains in a cosmological density field. The simulation has been obtained using a multi-phase SPH code particularly designed for the study of galaxy formation (Marri & White 2003) and galactic winds. The initial parameters are those for the Λ CDM model adopted so far, ($\Omega_0 = 0.3$, $\Omega_\Lambda = 0.7$, $\Omega_b h^2 = 0.028$, $\sigma_8 = 0.9$). The simulation uses 128^3 particles in a box of $10.5 h^{-1}$ comoving Mpc. A group finding algorithm has been used to identify dark matter halos and the star-forming galaxies associated to them. For a more detailed description of the simulation, we refer the reader to Bruscoli et al. (2003) and Maselli et al. (2004).

We investigated the sputtering process on the $z = 3.27$ simulation output. The particle properties have been mapped on a 3-D grid of 128^3 cells. For each cell, we derived gas density, temperature and ionization fractions for each of the chemical species by performing a standard SPH smoothing on the 32 particles nearest to each cell. The spatial resolution of the grid is $\approx 82 \text{ kpc } h^{-1}$ comoving ($\approx 27.5 \text{ kpc}$ physical). In total, 398 groups of particles have been identified as galaxies in the simulation box. The mass of dust in each galaxy has been derived from the baryonic mass, using the dust-to-baryonic mass ratio computed by Edmunds & Eales (1998). Again, we allow 10 per cent of the dust to be ejected from the virial radius⁸ As both the

⁸ In total, $2.7 \times 10^8 M_\odot$ of dust are injected into the simulation volume, corresponding, for the adopted dust distributions, to a total number of dust grains $N_g = 1.6 \times 10^{55}$. We have run simulations with $N_p = 10^9$ packets of 1.6×10^{46} grains each. This is sufficient for the results presented in this section to be independent of N_p (i.e. Fig. 8 to 12 are not affected by simulation cells

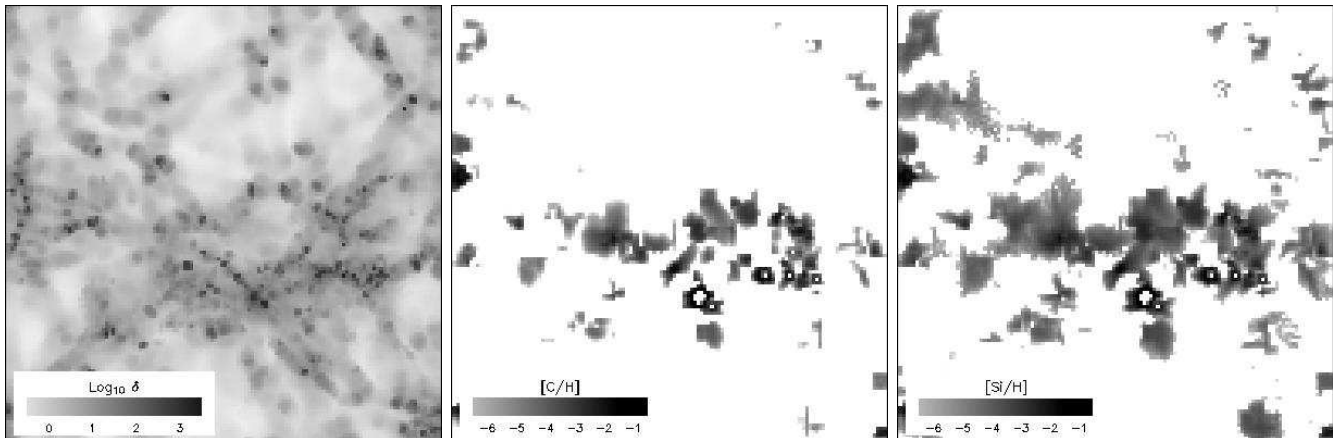


Figure 8. Cuts through the simulation box. The left panel shows the gas overdensity, while the centre and right panels show the carbon and silicon metallicities, respectively. The side of each map is $10.5h^{-1}$ comoving Mpc, 3.5 physical Mpc at $z = 3.27$. The unpolluted (white) cells in the [C/H] and [Si/H] maps are internal to the virial radius of the most massive galaxies in the selected slice.

dust-to-baryonic mass ratio and the fraction of dust ejected are considered to be upper limit, we believe the metallicity results obtained in this paper (which scale with the number of ejected grains) to be upper limits to the dust contribution to the IGM pollution. The virial radius is computed from the mass of the halo associated to each galaxy, as specified in § 4. Less massive galaxies are obviously more represented, with 80 per cent of the sample having a baryonic mass between $8.5 \times 10^8 M_{\odot}$ (the minimum mass) and $3.0 \times 10^9 M_{\odot}$ (and a dark matter mass roughly 10 times that value). As we said in § 4, a galaxy of *median* mass ejects into the IGM $3 \times 10^5 M_{\odot}$ of dust. Smaller objects also have virial radii which are quite close to the cell resolution (the halo of the smallest object has roughly the volume of a single cell).

In Fig. 8 we show a cut through the whole simulation box, parallel to one of the box faces. The map in the left panel refers to the gas density field; the metallicity maps in the central and right panel ([C/H] and [Si/H], respectively) are the results of the calculations described in this paper. As discussed previously, the drag has a smaller effect on the heavier and less charged silicate grains. This is evident in the larger area of the slice polluted with silicon. The slice passes through the most massive galaxy in the simulation (with baryonic mass $7 \times 10^{11} M_{\odot}$) which can be identified in the metallicity maps with the largest "hole" (inside a high metallicity region). The holes are the regions within the halo of each galaxy, that are excluded from the simulation (as grains are assumed to move from the virial radius *outward*). For the largest galaxy, $R_V=70$ kpc physical (2.5 times the dimension of a cell). Other high mass objects can be seen to the right. It is interesting to note how the massive galaxies are not necessarily surrounded by a wider metal enriched area, despite injecting into the IGM a larger amount of dust. As they reside in denser gas, grains ejected from these objects are more easily stopped by the drag.

In Fig. 9, we show the metallicity as a function of the gas overdensity. Each dot in the left (right) panel represents a simulation cell which has been polluted by carbon (silicon)

where only a few grain has passed and thus not having converged to a mean value for the metallicity, grain density and number).

as the result of the passage of one or more graphite (silicate) grains. As a reference, in the left panel we have plotted the median carbon metallicity ($\pm 1\sigma$ of lognormal scatter) derived by Schaye et al. (2003) as a function of the gas overdensity (gray area). We are showing the value at $z = 2$. In the right panel, the same area is indicated, but scaled for the [Si/C] ratio measured by Aguirre et al. (2004) for gas with $\delta > 3$. Similar metallicity levels have been reported by Simcoe et al. (2004), by fitting hydrogen and metal lines at $z = 2 - 2.5$ in QSO's absorption spectra. They do not detect a significant trend with the gas density. However, this may be due to the different choice for the UV background needed to correct for ionization, as harder spectra lead to a shallower dependence on δ (Schaye et al. 2003).

As seen in the homogeneous case, grain sputtering can produce non negligible metallicities in the IGM gas. The dependence of metallicity on density is steeper than what inferred from observations. Most cells with $\delta \approx 1$ have [C, Si/H] ≈ -5 , approximately one order of magnitude lower than the values measured by Schaye et al. (2003) and Aguirre et al. (2004) (especially [C/H]). The contribution of dust sputtering becomes more important for moderately overdense gas with $\delta = 10 - 100$, which can be translated in the neutral hydrogen column density range $14.5 < \log N(\text{H I}) < 16$. We find, however, that only 4-5 per cent of the cells in this overdensity range have [Si,C/H] values within the observationally allowed area. We remind that we believe this to be an upper limit, both for the total amount of dust and for the relative number of silicate and graphite grains ejected into the IGM (we use a 1:1 ratio). If the fraction of silicate grains is smaller, as some works seem to suggest (§ 2), [Si/H] would be smaller. However, the trend with density will be the same. While the level of metallicity in our simulations scales with the ejected mass of dust, the value derived by Schaye et al. (2003) depends on their assumption for the UV background. The scatter, instead, depends less on the assumptions and more on the underlying physics and on the density structure of the IGM (Aguirre, private communication). For cells with $\delta \approx 1$, we find a log-normal scatter of about 1.6 dex (slightly larger for Si). This is about twice what inferred from observations.

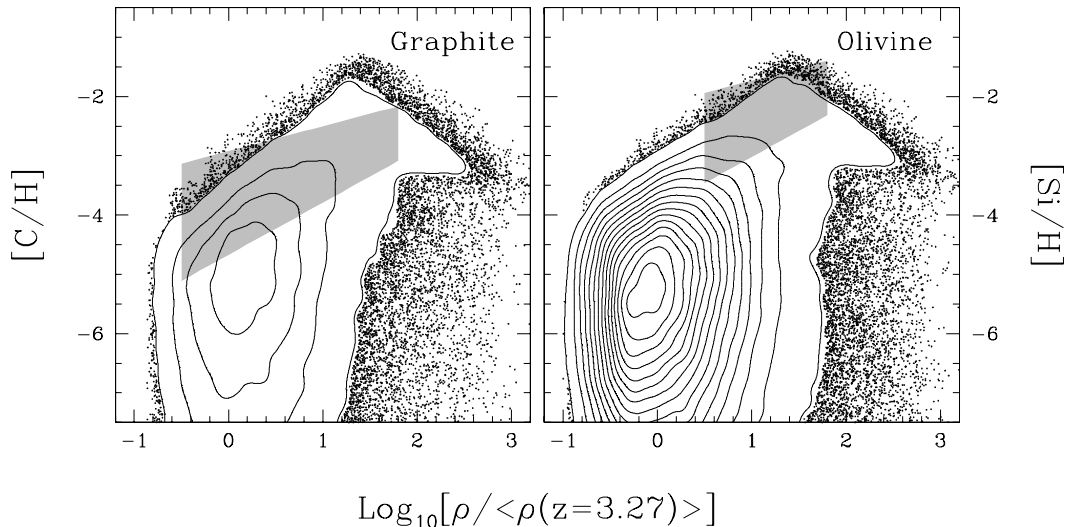


Figure 9. Metallicity vs overdensity for simulation cells polluted by carbon from graphite grains (left) and silicon from olivine grains (right). Each cell is indicated by a dot. Contours are plotted for regions where the density of dots becomes high. In both panels, contours start at 20 (and increase by 40) cells per 0.1 dex in overdensity and metallicity. The gray area refers to the metallicity measurements of Schaye et al. (2003) and Aguirre et al. (2004).

The features in the scatterplot reflect the movement of dust grains. In each panel, the region in the top-right is occupied by cells *just outside* the virial radius of the injecting galaxies, where the grain movement starts. In principle, for an isolated halo, gas at R_V has $\delta \approx 60$ (Navarro et al. 1997). However, due to the complex IGM structure and to the lack of resolution, the gas cells where the grain movement starts have overdensities $1 \lesssim \log_{10}(\delta) \lesssim 3$ (we will comment on resolution in § 6). Because of the high density and grain velocities, metallicities (and sputtering rates) are high in these cells. As the grain moves towards the less dense gas, it is slowed down by gas drag. For reduced velocities and gas densities, the sputtering rates are lower and so the resulting metallicities. This explains the general trend from high ρ - high metallicity to low ρ - low metallicity seen in both panels of Fig. 9. The slope of the relation depends both on the initial grain velocity and radius (as seen for the homogeneous case of § 4) and on the gas density.

There are some exceptions to such trend. Grains ejected into the higher density gas are stopped by drag more efficiently and pollute a smaller region around them. This is why the high metallicity cells at $\delta > 2$ appear isolated (i.e. with no contiguous lower metallicity and δ points) in the scatterplot. As the velocity quickly reduces within the dense region, some high- δ cells end up with low metal pollution. In this case the slope of the relation becomes very steep and lack of resolution limits the detailed study. Other low metallicity cells with high- δ mark the end-point of grains previously travelling in a less dense environment that stop as they cross a denser filament in the density field.

The gas which grains encounter as they leave a galaxy is often shock-heated by gravitational collapse and/or SNe. The cells with the highest metallicities in Fig. 9 have temperatures in excess of 10^5 -K. However, this has little effect on the metallicity levels: the grain initial velocities considered here are always higher or close to those delimiting the non-thermal regime for sputtering. Instead, the high temperature

determines the mechanism responsible for the drag. In the hot gas, collisional drag is more important (§ 3.1) and the grain movement does not depend on the charge. Coulomb drag becomes more important than collisional drag in the low temperature gas close to $\delta=1$ and it is because of it that grains come to a halt. Within the adopted simulation time t_f , most grains are slowed down and have energies below the threshold energy for sputtering. Even a ten-fold increase in t_f does not change the results significantly.

By counting cells which have been polluted, we can provide an estimate for the volume filling factors of metals. A wider volume is polluted by silicon, and this is clearly shown by the larger number of points (cells) in the right panel of Fig. 9 (and by the map in Fig. 8). By checking simulations with increasing number of grain packets, we found that the silicon filling factor tends asymptotically to about 18 per cent. As most of the cells are occupied by low density gas far from sources, filling factors are obviously higher for denser regions. When considering all cells with overdensity $\delta > 10$, the silicon filling factor increases to 40 per cent. The mean filling factor of cells polluted with carbon is a factor three lower (≈ 6 per cent). Thus, the distribution of metals in our simulations is rather inhomogeneous. Though a fraction of cells in Fig. 9 have metallicities compatible with the median value of Schaye et al. (2003), the median metallicity in our simulation is zero, for any gas density bin.

As Fig. 9 clearly show, the ratio $[\text{Si}/\text{C}]$ in our simulation is lower than 0.77 ± 0.05 , the value inferred by Aguirre et al. (2004) at $z \approx 3$ for gas with $\delta \gtrsim 3$. In the high density gas, $[\text{Si}/\text{C}]$ depends mostly on the assumption about the relative number of silicate/graphite grains and on the differences between the sputtering yields. If a cell is crossed by the same amount of both kind of grains, and if the kinetic energy is above the sputtering threshold, the ratio is quite constant. For example, silicate and graphite grains travelling at 500 km s^{-1} in the same cell would pollute the gas to $[\text{Si}/\text{C}] \approx 0.15$. Indeed, the high density cells where the grain

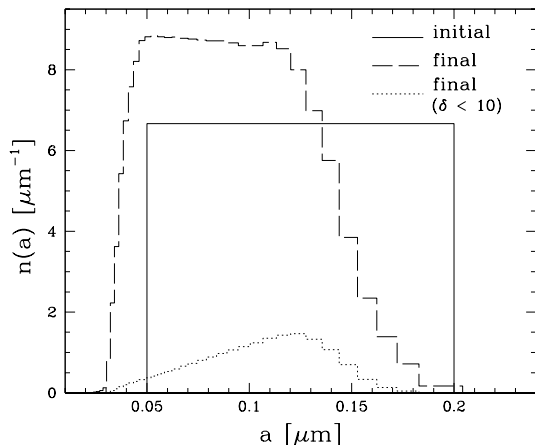


Figure 10. Initial (solid line) and final (dashed line) grain size distributions. The two histograms have been normalised to unity. The distribution for grains at rest in gas with $\delta < 10$ is shown with a dotted line (about 10 per cent of the total).

movement starts have $[\text{Si}/\text{C}] \approx 0.1 \pm 0.08$. Again, a comparison between the scatter in simulations and that derived from observations may be less dependent on the assumptions that have been made: for the high density cells, the scatter is similar to that of Aguirre et al. (2004), while it increases at lower density. The $[\text{Si}/\text{C}]$ value increases as well at lower δ , because olivine grains keep higher velocities to larger distances (for our assumptions, 3 per cent of the simulated volume has $[\text{Si}/\text{C}] > 1$).

During their travel, dust grains are eroded but never destroyed by sputtering. At the end of the simulation, dust grains at rest are present throughout all the volume polluted with metals (the filling factors of metal polluted cells and cells containing grains at rest are similar). The final size distribution (Fig. 10) is roughly flat, as the input one, but with a different range in radii. The smallest grains have radii $a \approx 0.02\text{-}\mu\text{m}$ and originate from particles with initial radius $a = 0.05\text{-}\mu\text{m}$, while largest grains reduce their radius from $a = 0.2\text{-}\mu\text{m}$ to $a = 0.15\text{-}\mu\text{m}$ ⁹. The latter are the grains that contribute mostly to metal pollution and, as we discussed previously, travel farther out from their injection point: for regions of diffuse gas ($\delta < 10$) the grain distribution is peaked around sizes $0.1\text{-}0.15\ \mu\text{m}$. There is no significant difference between graphite and silicate grains.

In Fig. 11, we show the final grain density (both silicate and graphite) as a function of the gas overdensity, for cells occupied by dust grains at rest. Features corresponding to those of Fig. 9 can be noticed. The higher grain densities, corresponding to higher gas densities, are due to a relatively large number of grains that stop close to the injection point. Only a limited number of grains travel far out, and this makes for the reduction of grain density for $\delta < 10$.

Inoue & Kamaya (2004) derived an upper limit for the dust grain density. After adopting various cosmic star formation histories (to account for the dust generation) they

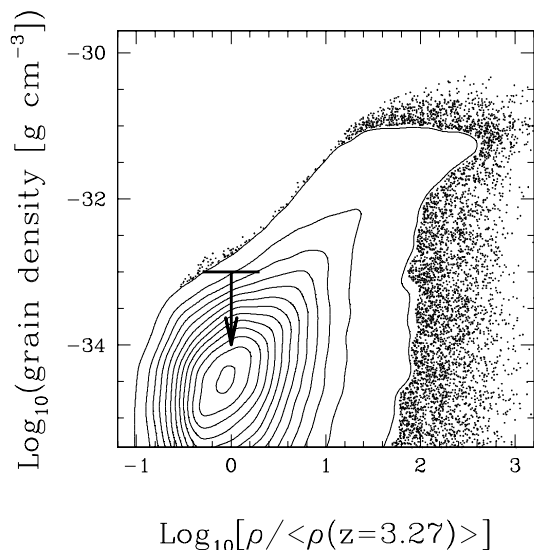


Figure 11. Dust grain density in the IGM vs gas overdensity for simulation cells occupied by grains at rest. Each cell is indicated by a dot. Contours are plotted for regions where the density of dots becomes high; they start at 20 (and increase by 80) cells per 0.1 dex in overdensity and grain density. The upper limit refers to the results of Inoue & Kamaya (2004).

constrained the amount of dust in the IGM at $\delta = 1$ with the maximum extinction and reddening allowed by the (now preferred) cosmological explanation for the dimming of high- z Type Ia SNe. Furthermore, they tightened the constraint requiring that dust grains cannot significantly alter, via photoelectric heating, the thermal history of the IGM derived from the low column density lines of the Ly α forest (Schaye et al. 2000). The upper limit for grains of size $a = 0.1\text{-}\mu\text{m}$ is plot in Fig. 11. The median density for $\delta = 1$ cells occupied by grains is about 1.5 orders of magnitude lower than the upper limit. As for metallicity, the results of Fig. 11 scale linearly with the amount of dust ejected in the IGM. If our upper limits are correct, the extinction and heating effects of IGM grains are not likely to be detected.

6 COMPARISON WITH PREVIOUS WORKS

Aguirre et al. (2001a,c) found that dust expulsion and erosion can account for the observed levels of carbon and silicon enrichment in the IGM. Since there are several differences between their work and ours, it is not easy to compare the results. They position grains at a distance from the galaxy where gravitation is balanced by radiation pressure. Because of this, silicate grains (having a larger material density) do not lay as far out as graphite grains. Furthermore, silicate grains have a smaller efficiency for radiation pressure. This is opposite to our results, where heavier silicate grains can travel to larger distances. They adopt essentially a power law distribution for grain sizes. Grains with radii $a = 0.03 - 0.05\ \mu\text{m}$ have larger equilibrium distances than grains with $a > 0.1\text{-}\mu\text{m}$. Again, this is opposite to what we find here by studying the dynamics of grains.

Another difference is in the amount of dust that is ejected. Aguirre et al. allow half of the metal content of each galaxy in their simulation to be distributed in the IGM as

⁹ Incidentally, by using TRIM Gray & Edmunds (2004) have found that sputtering does not simply lead to grain erosion: the stopping of projectiles into the material may change the structure and composition of the grain, especially in a metal rich gas

dust. As typically only half of a galaxy’s metal mass is believed to be in dust, this is equivalent to ejecting the whole dust content from the galaxy. Although we believe that 10 per cent is an upper limit to the fraction of dust ejected into the IGM (see § 2), even allowing all the dust mass to travel to the IGM (with large grains overrepresented with respect to the standard MRN power law) does not change significantly the results. As it can be seen by simply shifting upward by 1 dex the metallicities of Fig. 9, more metal polluted cells will lay within the range derived from observations. Still, the filling factor of metal polluted cells will not change. The same shift applies to the points of Fig. 11. Even increasing by one order of magnitude the grain density, the limit set by Inoue & Kamaya (2004) will not be violated in most cells with grains at rest.

The distribution of metals in our simulations is inhomogeneous, with filling factors smaller than 0.5 for any gas density bin, and it seems smaller than that in Aguirre et al. (2001a,c) (we compare our results to their case in which only the metals effectively eroded from grains are considered). One potential interpretation is that in our simulation the IGM density field has been “frozen” at $z = 3$, where all grains have been ejected. The 40 per cent decrease of the mean density from $z = 3$ to $z = 2$ (the end of the simulation) it is however unlikely to produce significantly different effects. The lowest mass galaxies in our simulations have halos of the same size as the cells. Lacking higher spatial (and density) resolution, grains ejected from small galaxies at the virial radius may find themselves in a denser environment than expected. As both these issues concern the movement of grains in less dense environments, we ran a simulation in which grains were injected at a distance from each galaxy *twice* the virial radius. The metallicity-density plot for this test simulation is shown in Fig. 12. Now the cells where the grain movement starts have a slightly lower density (there are less atoms to collide with) and obviously have lower metallicity (the peak of its distribution is shifted towards $\delta \approx 1$). The reduction in gas particles also mean a smaller drag and a smaller reduction in velocity as the grain moves. The slope of the metallicity-density trend in Fig. 12 becomes flatter, and closer to the data of Schaye et al. (2003). Also, a good fraction of $\delta \approx 1$ cells has now metallicities within the shaded area (at least for [C/H]). There is also an obvious increase in the filling factors, with silicon being present in 50 per cent of the volume, and carbon in 20 per cent. Similar trends can be seen in the grain density distribution, with an increase of the density by about 0.2 dex for cells with $\delta < 1$ (a reduction by 0.2 dex for $\delta > 10$). Clearly, a better spatial resolution is desirable, although the conclusions are not going to be substantially altered.

Finally, we note here that it would be possible to obtain higher metallicity levels by destroying completely the grains, via some unknown mechanism other from thermal/non-thermal sputtering. In our simulation a sizable fraction of large grains are at rest in gas with $\delta < 10$. By adding their contribution in atoms to the metallicity produced by the sputtering processes we have considered, we would rise by almost 2 dex the metallicity of one third of cells at $\delta < 1$, while leaving metallicity levels unaltered for $\delta > 10$.

7 SUMMARY AND CONCLUSIONS

We have analysed the motion of dust grains in the $z = 3$ IGM, to study the erosion due to sputtering and the subsequent pollution of the gas with metals. A fraction of the dust grains in a galaxy are thought to escape the gravitational well because of radiation pressure from starlight. Using results in the literature, we have defined plausible distributions for the sizes and velocities of the escaping grains. Our fiducial grain size distribution is flat, with radii in the range $0.05 < a[\mu\text{m}] < 0.2$, as literature results suggest that only large grains can escape from galaxies. The assumed velocity distribution is flat as well, with $100 < v[\text{km s}^{-1}] < 1000$. For such velocities, grains are supersonic under most of the gas conditions explored: thus, *non-thermal* sputtering is the dominant mechanism for the grain erosion.

The motion of each ejected grain is studied from the virial radius, until the velocity becomes small and the grain stops. Our computation takes into account:

(i) a calculation of the grain charge, due to collisions with electrons and ions in the IGM plasma and to photoejection of electrons by a metagalactic UV background. We have used the Bianchi et al. (2001) UV background including the contribution of galaxies and taken into account the velocity dependence of the collisional charging rates;

(ii) the gas drag, including both the collisional term and the Coulomb term due to interaction of the (heavily) charged grain in the $z = 3$ gas and the charged particles in the gas;

(iii) the sputtering of atoms off the grain surface, due to collisions with the ions in the IGM. Using the code TRIM, we have derived new sputtering yields for H and He atoms colliding with graphite and a silicate, olivine. Analytical fits to these yields are provided. The new yield have been compared to the widely used yields of Draine & Salpeter (1979).

The grain motion has been studied for a single source of grains (galaxy) in a homogeneous density field and inside a cosmological simulation, allowing the galaxies detected in the simulation box to eject 10 per cent of their dust mass into the IGM. We believe this assumption (as well as the resulting metallicities and grain density) to be an upper limit, compatible with the presumable MRN-like dust distribution inside a galaxy and the adopted size distribution for ejected grains. The motion is followed for 1 Gyr (half the Hubble time at $z = 3$), allowing us to compare our results to observations at $z = 2$. The main results are:

(1) Only large ($a \gtrsim 0.1\text{-}\mu\text{m}$) grains can reach out for the low density regions in the IGM, because the drag is less effective for heavier grains. For the same reason, silicate grains are able to diffuse in the IGM more than graphite grains and pollute with metals a larger fraction of the cosmic volume. Carbon and silicon metallicities produced by dust sputtering of graphite and olivine grains show a well defined trend with gas density. High density cells in the vicinity of galaxy halos (where the grains start their travel) have high metallicities, whereas fewer grains (originally at high v) reach gas with $\delta \approx 1$, with reduced velocity producing smaller sputtering rates. Those grains that are able to reach lower density regions are stopped, within the simulation time, by Coulomb drag. None of the large grains is completely destroyed by sputtering. The results summarised in this point are general and do not depend on the assumption on the adopted size

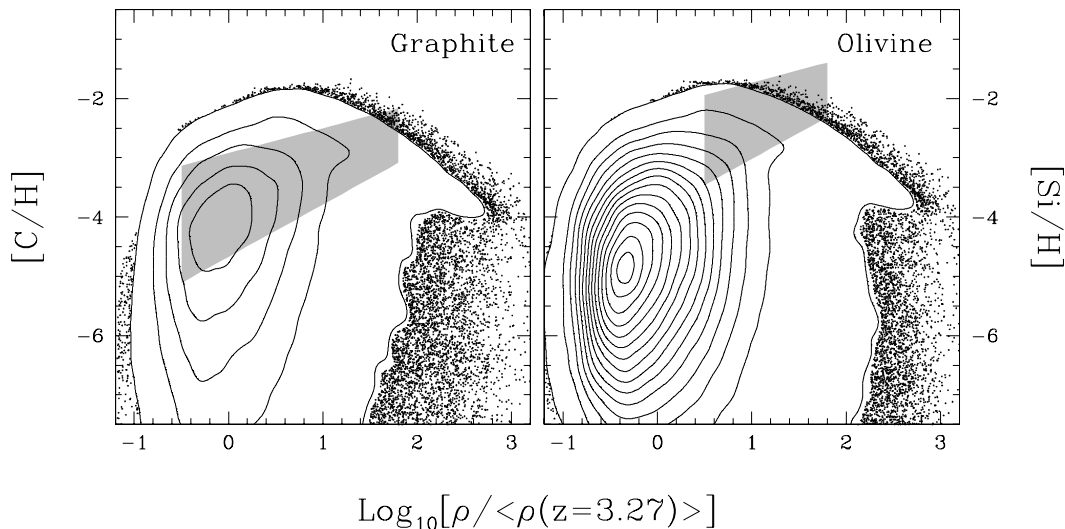


Figure 12. Same as Fig. 9, but ejecting dust grains at a distance from each galaxy *twice* the virial radius. In these figure, contours start at 20 (and increase by 160) cells per 0.1 dex in overdensity and metallicity.

and velocity distribution and fraction of dust mass ejected from galaxies, nor on the specific density field used in this work.

(2) For our parameter choice, most of the $\delta \approx 1$ simulation cells polluted with metals have $[C, Si/H] \approx -5$, approximately one order of magnitude lower than the median values recently derived by Schaye et al. (2003) and Aguirre et al. (2004). The contribution of dust sputtering becomes more important for moderately overdense gas with $\delta = 10 - 100$, corresponding to neutral hydrogen column densities $14.5 < \log N(H I) < 16$. For this overdensity range, however, only 4 per cent of the cells have $[C/H]$ values within the observationally allowed area. For any density bin, metallicities have a large scatter (a lognormal $\sigma > 0.15$ dex at $\delta \approx 1$). This is twice what has been inferred from observations of absorption lines. In addition, we recall that olivine grains pollute the IGM with Fe, Mg (same level as $[Si/H]$), and oxygen ($[O/H]$ is a factor four higher than $[Si/H]$), although these species are less readily observed in the IGM.

(3) Polluted cells in the range where dust sputtering is important ($10 < \delta < 100$) tend to have $0 \lesssim [Si/C] \lesssim 0.2$, almost independently of the gas density. The value we have obtained strongly depend on the graphite/silicate proportion, which we have assumed to be 1:1, as for MRN dust. If this is correct, we would have $[Si/C] \lesssim 0.2$ when allowing for a lower ejection efficiency of silicate grains with respect to graphite (as suggested by a few work in the literature). Such ratio is substantially smaller than the nucleosynthetic one, approximately equal to 0.9. Hence, this ratio might represent a valuable tool to assess the importance of the grain sputtering enrichment by systematic searches and studies of low $[Si/C]$ absorption systems.

(4) Resulting metal distributions are very inhomogeneous, with only 18 per cent of the volume occupied by cells polluted with silicon (from far-reaching olivine grains) and 6 per cent with carbon. These results slightly depend on resolution, but we estimate that filling factors larger than 50 per cent (for silicon) for cells at $\delta = 1$ enriched by dust sputtering are unlikely.

(5) Even allowing all dust mass produced inside galaxies by $z = 3$ to be ejected, the grain density in the low ($\delta \approx 1$) density IGM is below the upper limit derived by Inoue & Kamaya (2004), from IGM thermal history and extinction considerations. However, some moderately dense regions with $\delta > 10$ might contain a significant amount of dust, whose extinction effects remain to be calculated in detail.

To conclude, our results show that radiation-pressure driven dusty flows, followed by sputtering of the grains, might represent a viable and attractive mechanism to enrich the IGM with (cool) heavy elements. This process mostly affects moderately overdense IGM, without affecting too much the low-density gas: this is understood by the enhanced sputtering efficiency where the gas density is higher.

At least, three aspects of the problem need further study before we can draw final conclusions. The first concerns the ejection of dust grains from galaxies: although a few authors have studied the problem (we have used their results here as initial conditions) so far no work presents a detailed statistical analysis of the properties of escaping grains. In particular, estimates are lacking for the fraction of the dust mass which is ejected, as a function of the dust size and composition and of the galactic mass. This is important if we want to study the history of dust ejection and metal pollution by grain sputtering. At redshift $z > 3$, despite an higher IGM density (increase in the drag), the physical distance between galaxy is smaller and grains may be able to pollute a larger volume of the universe. However, galaxies have a smaller stellar mass: if the internal radiation field is weaker, the dust ejection efficiency may be reduced (unless this effect is contrasted by changes in the ISM drag and in gravity). The second aspect relates to the UV background fluctuations: in this study we have considered the UVB to be isotropic. However, radiative transfer effects (as shadowing and shielding), in the vicinity of galaxies or dense cosmic filaments, might create anisotropies resulting in a net radiation force on the grain. Such force might be large enough to prevent the grain from stopping as it currently happens in our simulations. In this case, the grain can continue to

move essentially taking a random walk, until it enters a regions of very high density (for example an accreting flow) within which it becomes fully coupled to the gas. If so, more metals could be released and less grains would survive, thus further decreasing the resulting intergalactic extinction. The third important effect concerns the intergalactic magnetic fields, which we have so far ignored. Although they might not be generally dynamically important, they might affect dust sputtering, via the betatron effect. We plan to focus on these additional physical effects in forthcoming papers.

ACKNOWLEDGMENTS

SB would like to thank the European Southern Observatory, where this project started, and the Osservatorio Astrofisico di Arcetri (OAA), for hospitality during the early phases of the work. AF acknowledges the affiliation to the OAA. We are grateful to A. Inoue and A. Aguirre for profitable discussions, to L. Del Zanna and S. Landi for their help with computational issues, and to an anonymous referee for comments that significantly improved the paper. This work was partially supported by the Research and Training Network "The Physics of the Intergalactic Medium" set up by the European Community under the contract HPRN-CT2000-00126 RG29185.

REFERENCES

- Aguirre A., 1999a, *ApJ*, 525, 583
Aguirre A., Hernquist L., Katz N., Gardner J., Weinberg D., 2001a, *ApJL*, 556, L11
Aguirre A., Hernquist L., Katz N., Gardner J., Weinberg D., 2001b, *ApJ*, 560, 599
Aguirre A., Hernquist L., Katz N., Gardner J., Weinberg D., 2001c, *ApJ*, 561, 521
Aguirre A., Schaye J., Kim T., Theuns T., Rauch M., Sargent W. L. W., 2004, *ApJ*, 602, 38
Aguirre A. N., 1999b, *ApJL*, 512, L19
Anders E., Grevesse N., 1989, *Geochimica et Cosmochimica Acta*, 53, 197
Baines M. J., Williams I. P., Asebiomo A. S., 1965, *MNRAS*, 130, 63
Barsella B., Ferrini F., Greenberg J. M., Aiello S., 1989, *A&A*, 209, 349
Bianchi S., Cristiani S., Kim T.-S., 2001, *A&A*, 376, 1
Bruscoli M., Ferrara A., Marri S., Schneider R., Maselli A., Rollinde E., Aracil B., 2003, *MNRAS*, 343, L41
Cowie L. L., Songaila A., 1998, *Nature*, 394, 44
Croft R. A. C., Davé R., Hernquist L., Katz N., 2000, *ApJL*, 534, L123
Davies J. I., Alton P. B., Bianchi S., Trewella M., 1998, *MNRAS*, 300, 1006
de Bernardis P., et al. 2000, *Nature*, 404, 955
Draine B. T., 1978, *ApJS*, 36, 595
Draine B. T., 1995, *ApSS*, 233, 111
Draine B. T., Lee H. M., 1984, *ApJ*, 285, 89
Draine B. T., Salpeter E. E., 1979, *ApJ*, 231, 77
Draine B. T., Sutin B., 1987, *ApJ*, 320, 803
Edmunds M. G., Eales S. A., 1998, *MNRAS*, 299, L29
Ellison S. L., Songaila A., Schaye J., Pettini M., 2000, *AJ*, 120, 1175
Ferrara A., 1997, in Lesch H., R.-J. D., Mebold U., Schlickeiser R., eds, *The Physics of Galactic Halos The Quest for Extragalactic Dust*. pp 189–
Ferrara A., Aiello S., Ferrini F., Barsella B., 1990, *A&A*, 240, 259
Ferrara A., Ferrini F., Barsella B., Franco J., 1991, *ApJ*, 381, 137
Field D., May P. W., Pineau des Forets G., Flower D. R., 1997, *MNRAS*, 285, 839
Flower D. R., Pineau des Forets G., Field D., May P. W., 1996, *MNRAS*, 280, 447
Gnedin N. Y., Ferrara A., Zweibel E. G., 2000, *ApJ*, 539, 505
Gray M. D., Edmunds M. G., 2004, *MNRAS*, 349, 491
Inoue A. K., Kamaya H., 2003, *MNRAS*, 341, L7
Inoue A. K., Kamaya H., 2004, *MNRAS*, 350, 729
James A., Dunne L., Eales S., Edmunds M. G., 2002, *MNRAS*, 335, 753
Jurac S., Johnson R. E., Donn B., 1998, *ApJ*, 503, 247
Madau P., Ferrara A., Rees M. J., 2001, *ApJ*, 555, 92
Marri S., White S. D. M., 2003, *MNRAS*, 345, 561
Maselli A., Ferrara A., Bruscoli M., Marri S., Schneider R., 2004, *MNRAS*, 350, L21
Mathis J. S., Ruml W., Nordsiek K. H., 1977, *ApJ*, 217, 425
May P. W., Pineau des Forêts G., Flower D. R., Field D., Allan N. L., Purton J. A., 2000, *MNRAS*, 318, 809
Montier L. A., Giard M., 2004, *A&A*, 417, 401
Nath B. B., Sethi S. K., Shchekinov Y., 1999, *MNRAS*, 303, 1
Navarro J. F., Frenk C. S., White S. D. M., 1997, *ApJ*, 490, 493
Northrop T. G., Birmingham T. J., 1990, *Planetary & Space Science*, 38, 319
Nozawa T., Kozasa T., Umeda H., Maeda K., Nomoto K., 2003, *ApJ*, 598, 785
Osterbrock D. E., 1989, *Astrophysics of Gaseous Nebulae and Active Galactic Nuclei*. University Science Book, Mill Valley
Perlmutter S., et al. 1999, *ApJ*, 517, 565
Riess A. G., et al. 1998, *AJ*, 116, 1009
Schaye J., 2001, *ApJ*, 559, 507
Schaye J., Aguirre A., Kim T., Theuns T., Rauch M., Sargent W. L. W., 2003, *ApJ*, 596, 768
Schaye J., Theuns T., Rauch M., Efstathiou G., Sargent W. L. W., 2000, *MNRAS*, 318, 817
Schneider R., Ferrara A., Salvaterra R., 2004, *MNRAS*, 351, 1379
Schneider R., Ferrara A., Salvaterra R., Omukai K., Bromm V., 2003, *Nature*, 422, 869
Shull J. M., 1978, *ApJ*, 226, 858
Shustov B. M., Vibe D. Z., 1995, *Astronomy Reports*, 39, 578
Simcoe R. A., Sargent W. L. W., Rauch M., 2004, *ApJ*, 606, 92
Simonsen J. T., Hannestad S., 1999, *A&A*, 351, 1
Spergel D. N., Verde L., Peiris H. V., Komatsu E., Nolte M. R., Bennett C. L., Halpern M., Hinshaw G., Jarosik N., Kogut A., Limon M., Meyer S. S., Page L., Tucker G. S., Weiland J. L., Wollack E., Wright E. L., 2003, *ApJS*, 148,

175

- Spitzer L., 1962, *Physics of Fully Ionized Gases*. Interscience, New York
- Spitzer L., 1978, *Physical Processes in the Interstellar Medium*. Wiley, New York
- Tielens A. G. G. M., McKee C. F., Seab C. G., Hollenbach D. J., 1994, *ApJ*, 431, 321
- Todini P., Ferrara A., 2001, *MNRAS*, 325, 726
- Vallée J. P., 2004, *New Astronomy Review*, 48, 763
- Weingartner J. C., Draine B. T., 2001a, *ApJ*, 548, 296
- Weingartner J. C., Draine B. T., 2001b, *ApJ*, 553, 581
- Weingartner J. C., Draine B. T., 2001c, *ApJS*, 134, 263
- Whittet D. C. B., 1992, *Dust in the Galactic Environment*. Institute of Physics Publishing, Bristol
- Ziegler J. F., Biersack J. P., Littmark U., 1985, *The Stopping and range of Ions in Solids*. Pergamon, New York